
This is an electronic reprint of the original article.
This reprint may differ from the original in pagination and typographic detail.

Lomanowski, B.; Rubino, G.; Uccello, A.; Dunne, M.; Vianello, N.; Aleiferis, S.; Canik, J.;
Carvalho, I.; Corrigan, G.; Frassinetti, L.; Frigione, D.; Garzotti, L.; Groth, M.; Meigs, A.;
Maslov, M.; von Thun, C. Perez; Rimini, F.; Schneider, P. A.; Sergienko, G.; Simpson, J.; Van
Eester, D.; JET Contributors

Parameter dependencies of the separatrix density in low triangularity L-mode and H-mode JET-ILW plasmas

Published in:
Nuclear Fusion

DOI:
[10.1088/1741-4326/aca9de](https://doi.org/10.1088/1741-4326/aca9de)

Published: 01/03/2023

Document Version
Publisher's PDF, also known as Version of record

Published under the following license:
CC BY

Please cite the original version:
Lomanowski, B., Rubino, G., Uccello, A., Dunne, M., Vianello, N., Aleiferis, S., Canik, J., Carvalho, I., Corrigan, G., Frassinetti, L., Frigione, D., Garzotti, L., Groth, M., Meigs, A., Maslov, M., von Thun, C. P., Rimini, F., Schneider, P. A., Sergienko, G., ... JET Contributors (2023). Parameter dependencies of the separatrix density in low triangularity L-mode and H-mode JET-ILW plasmas. *Nuclear Fusion*, 63(3), 1-22. Article 036019. <https://doi.org/10.1088/1741-4326/aca9de>

This material is protected by copyright and other intellectual property rights, and duplication or sale of all or part of any of the repository collections is not permitted, except that material may be duplicated by you for your research use or educational purposes in electronic or print form. You must obtain permission for any other use. Electronic or print copies may not be offered, whether for sale or otherwise to anyone who is not an authorised user.

PAPER • OPEN ACCESS

Parameter dependencies of the separatrix density in low triangularity L-mode and H-mode JET-ILW plasmas

To cite this article: B. Lomanowski *et al* 2023 *Nucl. Fusion* **63** 036019

View the [article online](#) for updates and enhancements.

You may also like

- [Basic physical processes and reduced models for plasma detachment](#)
P C Stangeby
- [Effect of carbon and tungsten plasma-facing materials on the divertor and pedestal plasma in EAST](#)
Chen Zhang, Chaofeng Sang, Liang Wang et al.
- [Simulation study of the influence of upstream density and power in the scrape-off layer on the double-peaked density profile at the divertor target](#)
Jin Guo, Shifeng Mao, Guozhang Jia et al.

Parameter dependencies of the separatrix density in low triangularity L-mode and H-mode JET-ILW plasmas

B. Lomanowski^{1,*} , G. Rubino² , A. Uccello³ , M. Dunne⁴ , N. Vianello⁵ , S. Aleiferis⁶ , J. Canik¹ , I. Carvalho¹³ , G. Corrigan⁶ , L. Frassinetti⁷ , D. Frigione⁸ , L. Garzotti⁶ , M. Groth⁹ , A. Meigs⁶ , M. Maslov⁶ , C. Perez von Thun¹⁰ , F. Rimini⁶ , P.A. Schneider⁴ , G. Sergienko¹¹ , J. Simpson^{6,9} , D. Van Eester¹²  and JET Contributors^a

¹ Oak Ridge National Laboratory, Oak Ridge, TN 37831-6169, United States of America

² University of Tuscia, DEIM, Via del Paradiso 47, 01100 Viterbo, Italy

³ Istituto per la Scienza e Tecnologia dei Plasmi, CNR, via Cozzi 53, 20125 Milan, Italy

⁴ Max Planck Institut für Plasmaphysik, Garching, Germany

⁵ Consorzio RFX (CNR, ENEA, INFN, Università di Padova, Acciaierie Venete SpA), Corso Stati Uniti 4, 35127 Padova, Italy

⁶ CCFE, Culham Science Centre, Abingdon OX14 3DB, UK

⁷ Fusion Plasma Physics, EES, KTH SE-10044 Stockholm, Sweden

⁸ Unità Tecnica Fusione, ENEA C. R., Frascati, via E. Fermi 45, 00044 Frascati, Roma, Italy

⁹ Aalto University, PO Box 14100, FIN 00076 Aalto, Finland

¹⁰ Institute of Plasma Physics and Laser Microfusion (IPPLM), Hery Str 23, 01-497 Warsaw, Poland

¹¹ Forschungszentrum Jülich GmbH, Institut für Energie- und Klimaforschung - Plasmaphysik, 52425 Jülich, Germany

¹² Laboratory for Plasma Physics, Koninklijke Militaire School—Ecole Royale Militaire, Renaissancelaan 30 Avenue de la Renaissance, B-1000 Brussels, Belgium

¹³ ITER Organization, Route de Vinon-sur-Verdon, CS 90 046, 13067 St. Paul Lez Durance Cedex, France

E-mail: lomanowskiba@ornl.gov

Received 5 August 2022, revised 21 November 2022

Accepted for publication 8 December 2022

Published 9 February 2023



CrossMark

Abstract

The midplane electron separatrix density, $n_{e,sep}$, in JET-ILW L-mode and H-mode low triangularity deuterium fuelled plasmas exhibits a strong explicit dependence on the averaged outer divertor target electron temperature, $n_{e,sep} \sim T_{e,ot}^{-1/2}$. This dependence is reproduced by analytic reversed two point model (rev-2PM), and arises from parallel pressure balance, as well as the ratio of the power and momentum volumetric loss factors, $(1 - f_{cooling})/(1 - f_{mom-loss})$. Quantifying the influence of the $(1 - f_{cooling})$ and $(1 - f_{mom-loss})$ loss factors on $n_{e,sep}$ has been enabled by measurement estimates of these quantities from L-mode density (fueling) ramps in the outer

^a See Mailloux *et al* 2022 (<https://doi.org/10.1088/1741-4326/ac47b4>) for the JET Contributors.

* Author to whom any correspondence should be addressed.



Original content from this work may be used under the terms of the [Creative Commons Attribution 4.0 licence](https://creativecommons.org/licenses/by/4.0/). Any further distribution of this work must maintain attribution to the author(s) and the title of the work, journal citation and DOI.

horizontal, VH(C), and vertical target, VV, divertor configurations. Rev-2PM $n_{e,sep}$ estimates from the extended H-mode and more limited L-mode datasets are recovered to within $\pm 25\%$ of the measurements, with a scaling factor applied to account for use of $\langle T_{e,ot} \rangle$, an averaged quantity, rather than flux tube resolved target values. Both the $(1 - f_{cooling})$ and $(1 - f_{mom-loss})$ trends and recovery of $n_{e,sep}$ using the rev-2PM formatting are reproduced in EDGE2D-EIRENE L-mode-like and H-mode-like density scan simulations. The general lack of a divertor configuration effect in the JET-ILW $n_{e,sep}$ trends can be attributed to a significant influence of main chamber recycling, which has been shown in the EDGE2D-EIRENE results to moderate $n_{e,sep}$ with respect to changes in divertor neutral leakage imposed by changes in the divertor configuration. The unified $n_{e,sep}$ vs $\langle T_{e,ot} \rangle$ trends can, however, be broken if large modifications to the divertor geometry (e.g. complete removal of the outer divertor baffle structure) are introduced in the model. The more pronounced high-field side high density region formation in the VH(C) configuration with reduced clearance to the separatrix does not appear to have a significant influence on the outer midplane separatrix and pedestal parameters when mapped to $\langle T_{e,ot} \rangle$, although conditions at the inner midplane could not be assessed.

Keywords: separatrix density, divertor and main chamber recycling, two point model, SOL-pedestal-core integration

(Some figures may appear in colour only in the online journal)

1. Introduction

The purpose of this paper is to further elucidate the plasma parameter correlations with the outer target electron temperature in JET with the ITER-like wall (JET-ILW) reported in the companion paper [1], with a focus on the outer midplane (OMP) separatrix density scaling. The key point from these experimental observations is that changes in global and edge plasma parameters ($H_{98(y,2)}$, dimensionless collisionality ν^* , core density peaking $n_{e,0}/\langle n_e \rangle$, separatrix density $n_{e,sep}$) with variations in the D_2 fueling rate, heating power, and divertor configuration are unified into a single trend when mapped to $\langle T_{e,ot} \rangle$, the spatially averaged spectroscopically derived outer target electron temperature. We noted that the remarkably robust $H_{98(y,2)}$ trend with $\langle T_{e,ot} \rangle$ is connected to a strong inverse correlation between $\langle T_{e,ot} \rangle$, $n_{e,sep}$ and ν^* in predominantly neutral beam heated plasmas. Thus the established relationship between ν^* , $n_{e,0}/\langle n_e \rangle$ and core pressure (see [2] and references therein) can be linked directly to changes in the divertor recycling moderated by $\langle T_{e,ot} \rangle$, such that decreasing $\langle T_{e,ot} \rangle$ (increasing $n_{e,sep}$ and ν^*) via additional D_2 fueling leads to a degradation of plasma performance as a consequence of reduced $n_{e,0}/\langle n_e \rangle$, pedestal electron temperature, $T_{e,ped}$, and core pressure via electron temperature profile stiffness.

Given the importance of $n_{e,sep}$ as an interface parameter constraining the compatibility between plasma performance and divertor detachment, we focus in the present work on developing a consistent description of the relationship between divertor conditions and gas fueled (unseeded) edge plasma behavior. We examine the applicability and limitations of reduced models such as the reversed two-point model (rev-2PM) [3, 4] to describe the main physical processes governing the $n_{e,sep}$ scaling. We will address the observed primary dependence of $n_{e,sep}$ on $\langle T_{e,ot} \rangle$ and the apparent lack of divertor configuration dependence in the $n_{e,sep}$, $n_{e,sep}/n_{e,ped}$ and $H_{98(y,2)}$ vs $\langle T_{e,ot} \rangle$ trends shown in [1], which is perhaps surprising/

unexpected and counterintuitive given the differences in divertor target inclination and degree of closure.

Recent experimental and modelling studies of divertor geometry on DIII-D [5–7] have shown a clear influence of closure on the particle flux rollover point (onset of particle detachment) mapped to the OMP pedestal and separatrix densities. The geometry differences between the DIII-D lower single null (LSN) open geometry and upper single null closed and small angle slot divertors are more extreme than the range of available LSN divertor configurations on JET-ILW. We will show that the unified $n_{e,sep}$ vs $\langle T_{e,ot} \rangle$ trends can indeed be broken with a sufficiently large change in the divertor geometry, for example by removing the entire outer divertor structure in 2D edge plasma simulations such that the resulting geometry resembles the DIII-D LSN open divertor. In addition, we will infer from measurements and modelling that main-chamber recycling (MCR) plays a significant role in moderating the influence of the geometry dependent neutral leakage rates from the divertor on the OMP $n_{e,sep}$, and discuss the challenges in capturing these effects with the extended rev-2PM.

In ASDEX-Upgrade (AUG), a correlation between p_0 , the divertor neutral pressure, and $n_{e,sep}$ has been established empirically giving $n_{e,sep} \propto p_0^{0.31}$ [8]. Using the rev-2PM to relate the target ion flux to the recycling neutral flux and p_0 , the $n_{e,sep}$ scaling on AUG is developed by merging the unknown volumetric loss factors for power and momentum losses observed to depend mostly on p_0 through a regression analysis of AUG H-mode discharges [8, 9]. Similarly, Leonard *et al* [10] have used the rev-2PM with an explicit dependence on the outer divertor electron temperature instead of the target ion flux, to recover measurements of $n_{e,sep}$ within reasonable agreement over a range of I_p , B_t and P_{NBI} in DIII-D H-modes in a fixed LSN open geometry. A consistent rise in $n_{e,sep}$ was observed with decreasing divertor target electron temperature, measured with the divertor Thomson scattering system. The $n_{e,sep}$

trends were found to follow the rev-2PM scaling, but only if the volumetric radiated power losses were taken into account (pressure losses were assumed to be small). Thus, given the successful application of the rev-2PM in these previous studies to inform the $n_{e,sep}$ parameter dependencies, we will extend its use in interpreting the experimentally measured $n_{e,sep}$ in JET-ILW leveraging direct measurements of the volumetric momentum and cooling loss factors. Quantifying these factors is enabled by spectroscopically inferred outer target electron temperature measurements. We will consider the limitations of the rev-2PM in capturing 2D recycling distribution changes via different divertor configurations.

Whereas relatively strong $n_{e,sep}$ dependencies on p_0 and on $\langle T_{e,ot} \rangle^{-1/2}$ are observed on AUG and JET-ILW (see companion paper [1]), respectively, SOLPS4.3 and SOLPS-ITER simulations of ITER baseline scenarios show a rather weak coupling between $n_{e,sep}$ and divertor neutral pressure owing to a projected improved compression of the recycled neutrals at the divertor targets [11]. Further numerical studies of ITER early operation phases indicate that the larger divertor size of ITER relative to AUG leads to better confinement of neutrals for equivalent ionization/dissociation mean free paths [12, 13]. The larger size of the JET-ILW divertor relative to DIII-D and AUG further motivates the interpretation of the $n_{e,sep}$ trends in JET-ILW supported by measurements and modelling, and is an important step in developing a machine size scaling of the degree of coupling between a dissipative divertor and $n_{e,sep}$.

The paper is organized as follows. Section 2 describes the L-mode and H-mode discharge datasets, as well as the EDGE2D and SOLPS-ITER simulation setups. Section 3 gives an overview of the extended 2PM for $n_{e,sep}$, followed by an analysis of measured and predicted cooling and momentum loss factors, which are important target electron temperature dependent parameters in the $n_{e,sep}$ model. In section 4 the measured $n_{e,sep}$ trends are recovered with the rev-2PM, and its applicability to JET-ILW divertor configurations and more generally its limitations with respect to large changes in divertor geometry are discussed. In section 5 the apparent absence of a clear divertor configuration dependence on $n_{e,sep}$ trends when mapped to the outer target electron temperature are further examined utilizing 2D edge plasma simulations. The influence of divertor closure, target inclination, high field side (HFS) high density formation and MCR on $n_{e,sep}$ are explored, followed by conclusions in section 6.

2. Methodology

The experimental setup, discharge dataset, and diagnostic methods are presented in [1], including a description of the spatially averaged, outer target spectroscopic measurements of the electron temperature, $\langle T_{e,ot} \rangle$ in different divertor configurations. Briefly, the dataset is comprised of dedicated $I_p = 2$ MA, $B_t = 2.3$ T, $P_{NBI} = 16$ MW, $P_{ICRH} = 2$ –3 MW low- δ unseeded H-mode discharges in four different divertor configurations (see figure 1 in [1]), fueled primarily by toroidally distributed gas introduction modules located in the divertor. The divertor configurations studied in [1] as well as in the present work

are (a) VH(C) and VH(D) with the inner strike point (ISP) on the vertical tile and outer strike point (OSP) on tile 5 stack C and D, respectively; (b) VV with the ISP and OSP on vertical targets; (c) CC with the ISP and OSP in the inner and outer corners in close proximity to the pump entrances; and (d) VC(T6) with the ISP on the inner vertical target and OSP on top of tile 6 corresponding to the innermost excursion in a swept strike point scenario (see figure 1).

An expanded dataset of unseeded low- δ deuterium fueled discharges has also been compiled from the 2019–2020 JET-ILW experimental campaign spanning the range: $P_{NBI} = 9$ –25 MW, $P_{ICRH} = 2$ –5 MW, $I_p = 1.5$ –3.4 MA, $B_t = 1.7$ –3.5 T and $q_{95} = 3$ –3.4. OMP electron temperature and density profiles were obtained and time-averaged during inter-edge-localized mode (ELM) periods using the high resolution Thomson scattering (HRTS) system [14].

We also carried out dedicated L-mode density ramp discharges in the four divertor configurations to evaluate the quality of the spectroscopic $\langle T_{e,ot} \rangle$ measurements, as well as to facilitate an assessment of the volumetric pressure-momentum and cooling loss trends presented in section 4. The heating power in these discharges varied between 1.1 and 2.5 MW, with $I_p = 2$ –2.5 MA and $B_t = 2.3$ –2.5 T.

2.1. Edge plasma simulation dataset

To aid in the interpretation of the experimental results presented in [1], we have compiled existing EDGE2D-EIRENE [15] edge plasma simulations from [16, 17]. These simulations include low power ($P_{in} = 2.2$ –3.8 MW) unseeded density scans in deuterium-only plasmas in the VV and VH(C) divertor configurations, including scans with and without cross-field drifts due to $\mathbf{E} \times \mathbf{B}$ and $\mathbf{B} \times \nabla B$. Details on the simulation setups, including assumptions on prescribed radial transport coefficients corresponding to L-mode-like electron density and temperature profiles at the OMP, can be found in [16, 17]. These scans have been extended to include the CC(T6) divertor geometry, which approximates the corner-corner (CC) configuration, but with the OSP positioned on top of tile 6 rather than in the outer corner (see figure 1). This compromise enables computational convergence of the gridding tool Grid2D with a sufficiently wide scrape-off layer (SOL) to largely capture the e-folding length of the radial density and outer target ion flux profiles, while avoiding modification of the divertor baffle geometry. Additionally, while this geometry does not fully capture the enhanced closure that is a salient feature of the CC configuration, it permits the synthetic spectroscopic evaluation of $\langle T_{e,ot} \rangle$ (see [18, 19] for details) since the OSP is in view of the spectrometer, as is the case in experiment.

To evaluate the influence of the divertor geometry on neutral leakage from the divertor and MCR (see section 6), we have introduced an additional geometry, CC(T6)-open, in which the outer divertor baffle structure has been removed leading to a wide open divertor geometry (see figure 1), qualitatively similar to the DIII-D LSN divertor (e.g. [5]). Cross-field drifts in the CC(T6) and CC(T6)-open density scans were not included.

Although the above simulations sets feature L-mode-like radial transport coefficients and lower input power compared

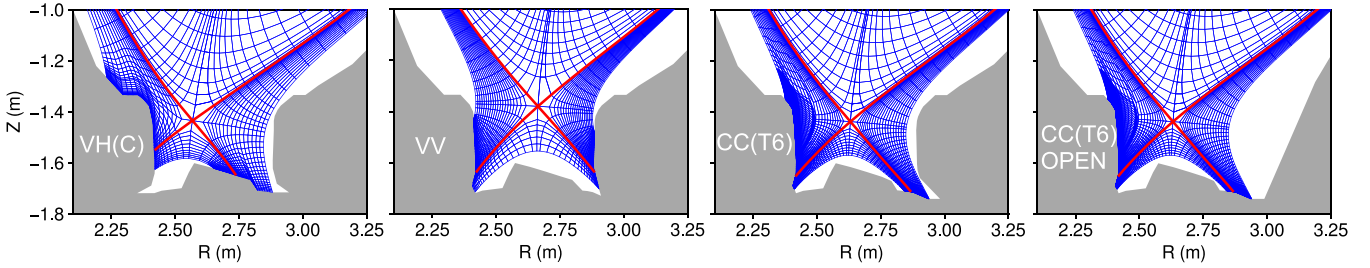


Figure 1. EDGE2D grids corresponding to the VH(C), VV, CC(T6) and CC(T6)-open divertor configurations. The CC(T6) configuration is a compromise in attempting to model the CC configuration by shifting the strike points towards the HFS affording a sufficiently large e-folding width to resolve the SOL upstream density and target particle flux profiles without modifications to the divertor baffle geometry. Note, EIRENE grid outside of the EDGE2D computational domain is not shown.

to the H-mode experiment dataset with variation in $P_{\text{NBI}} = 9\text{--}25$ MW, the ability to resolve drift effects combined with relative flexibility in numerical convergence of the plasma solutions made this dataset more accessible for evaluating trends spanning a wide $n_{e,\text{sep}}$ and $\langle T_{e,\text{ot}} \rangle$ range. To partially test the validity of the trends discussed in sections 4 and 5 to H-mode scenarios, density scans at $P_{\text{in}} = 14$ MW were also carried out for the VH(C) and VV configurations, albeit without cross-field drifts activated. These H-mode-like scans feature lower values of the fixed particle and thermal diffusion coefficients ($D_{\perp} = 0.05\text{--}0.15$ m² s⁻¹, $\chi_{e,i} = 0.5$ m² s⁻¹) at and near the separatrix, giving rise to a more pronounced transport barrier such that the resulting electron temperature and density profiles are matched to the HRTS profiles from the low recycling VV and VH(C) H-mode discharges with $P_{\text{NBI}} = 16$ MW and $P_{\text{ICRH}} = 2$ MW.

In addition to the EDGE2D-EIRENE density scans, we carried out L-mode-like density scans using the SOLPS-ITER code package [20] using the same set of grids for the VH(C) and VV configurations. The primary purpose of the SOLPS-ITER runs was to take advantage of built-in tools for decomposing the OMP ionization source profile by physical origin of the recycled neutrals, as discussed in section 6.2. The SOLPS-ITER density scans in VH(C) and VV yielded very similar plasma solutions to the corresponding EDGE2D-EIRENE simulations with the same set of radial transport coefficients and input power, thus giving confidence that the ionization profile decomposition is equally valid for the EDGE2D-EIRENE cases.

A notable limitation in both the L-mode-like and H-mode-like density scans is the assumption of constant radial transport coefficients with increasing $n_{e,\text{sep}}$. This simplistic approach is not consistent with tokamak experiments, where a collisionality dependence on radial particle fluxes has been observed [21], as well as turbulence driven widening of the near SOL electron temperature and density fall-off lengths [22], and the formation of flattened density profiles (density shoulders) in the far SOL [23, 24]. A more realistic treatment requires an adjustment of the radial transport coefficients informed by experimental observations, as has been demonstrated in [25] via a self-consistent collisionality dependent modification of D_{\perp} in the SOL of time-dependent EDGE2D density scan simulations, and in [26] by increasing the particle transport in the

SOL to more accurately fit experimental data corresponding to different time slices of an AUG L-mode density ramp discharge. Further modelling efforts are needed to incorporate and benchmark such heuristic models to capture the variation in the SOL radial transport coefficients.

3. Extended rev-2PM

The extended two-point model (2PM) [27, 28] has been widely used for relating the upstream pressure p_u , density n_u and parallel heat flux $q_{\parallel u}$, to the downstream target quantities n_t , T_t , and parallel particle flux $\Gamma_{\parallel t}$, along the same flux-tube, where the downstream quantities are often treated as the dependent variables and the upstream as the ‘driver’ quantities. Formulated using momentum and energy conservation equations in the SOL, the extended 2PM includes volumetric loss terms that capture the dissipative processes along flux tubes associated with momentum and cooling losses,

$$(1 - f_{\text{mom-loss}}) p_{\text{tot},u} = p_{\text{tot},t}, \quad (1)$$

$$(1 - f_{\text{cooling}}) q_{\parallel u} R_u = q_{\parallel t} R_t, \quad (2)$$

due to neutral-plasma collisional processes, impurity radiation and the net loss of energy and momentum from the flux tube due to cross-field transport (R_u and R_t —upstream and target major radius). $p_{\text{tot}} = (1 + M^2)n_e k T_e (1 + \tau)$ is the total pressure, $q_{\parallel t} = \gamma k T_{e,t} \Gamma_{\parallel t}$ the parallel heat flux at the target, where M is the Mach number, $\tau = T_i/T_e$, and $\gamma \approx 7$ is the sheath heat transmission coefficient, not including the potential energy contribution from surface ion recombination. The full description of the 2PM and expressions for $T_{e,t}$, $n_{e,t}$ and $\Gamma_{\parallel t}$ are provided in [3]. Our present focus is on the ‘reversed’ 2PM expression for the upstream electron density (equation (47) in [29]), obtained by rearranging equations (15b) in [3],

$$n_{e,u} = \left[\frac{\sqrt{8m_i}}{e^{3/2}\gamma} \left(\frac{2\kappa_{0e}}{7} \right)^{2/7} \right] \left[\frac{q_{\parallel u}^{5/7}}{T_{e,t}^{1/2} L^{2/7}} \right] \left[(1 + \tau_u)^{-1} \right] \times \left[\left(\frac{1 + \tau_t}{2} \right)^{1/2} \right] \left[\frac{(1 - f_{\text{cooling}})}{(1 - f_{\text{mom-loss}})(1 - f_{\text{conv}})^{2/7}} \right] \left[\frac{R_u}{R_t} \right], \quad (3)$$

in which $q_{\parallel u}$ at the OMP is assumed to be dominated by Spitzer parallel electron heat conduction, giving

$$T_{e,u} \approx \left(\frac{7(1-f_{\text{conv}})q_{\parallel u}L}{2\kappa_{0e}} \right)^{2/7}, \quad (4)$$

where $L \approx \pi Rq_{95}$ is the connection length, m_i is the fuel ion mass and f_{conv} is a correction factor for the convective fraction of $q_{\parallel u}$. Further assuming equal inter-ELM power sharing between the inner and outer divertor targets,

$$q_{\parallel u} = \frac{1/2P_{\text{SOL}}}{A} = \frac{1/2P_{\text{SOL}}}{2\pi R\lambda_q} \frac{|B|}{B_p}, \quad (5)$$

where λ_q is the power width, $P_{\text{SOL}} = P_{\text{in}} - P_{\text{rad,core}} - dW/dt$, $|B|$ and B_p are the total and poloidal magnetic field at the OMP, and dW/dt is the time derivative of the plasma stored energy. Due to the large variation in ELM size and frequency covered by the H-mode database, it was not possible to estimate dW/dt in a consistent manner, hence an ELM-averaged estimate of dW/dt was used for the P_{sol} estimate at high ELM frequency.

The power width, λ_q , can be estimated using the ITPA H-mode scaling [30] developed from multi-machine divertor heat flux data from a set of discharges in attached divertor conditions, giving $\lambda_q \propto (R/a)\rho_{s,\text{sol}}$, where $\rho_{s,\text{sol}} = (m_D T_{\text{sep}})^{1/2}/(eB_p)$ is the poloidal ion sound Larmor gyro-radius at the separatrix. This scaling has recently been revisited by Eich *et al* [22] to include high density discharges from AUG reaching the H-mode density limit, leading to a generalized power width scaling $\lambda_q \propto \rho_{s,\text{sol}}(1 + 2.1\alpha_t^{1.7})$, where $\alpha_t \propto q_{\text{cyl}}\nu_{ei}^*$ is a modified turbulence control parameter closely related to a normalized edge collisionality, ν_{ei}^* , but demonstrating a stronger dependence on the cylindrical safety factor, q_{cyl} . Most recent experimental results from TCV [31] incorporating the dependence of λ_q on α_t are also consistent with the AUG results. In comparison to the original ITPA λ_q scaling, the power width is shown to be broadened by up to a factor of three at high values of edge density with $\alpha_t \approx 1$.

The impact of this modified λ_q scaling, as well as the τ_t , τ_u and f_{conv} terms in equations (3) and (4) are discussed in section 5.2. Extension of the $\lambda_q(\alpha_t)$ scaling to JET is more challenging than on AUG as the method depends on high quality spatially resolved OMP T_e and n_e profiles in the SOL, hence no attempt is made here to verify this new scaling on JET. T_i/T_e ratios and the upstream parallel heat flux convective fraction are inferred from the EDGE2D density scans as these quantities are not available from experiment. We therefore proceed with a two-fold approach in applying the rev-2PM in an attempt to recover the measured $n_{e,\text{sep}}$:

(a) In the simplified treatment, ‘rev-2PM-simplified’, we use the established ITPA H-mode λ_q scaling from [30] to estimate $q_{\parallel u}$ and assume constant $\tau_u = 2$, $\tau_t = 1$, $f_{\text{conv}} = 0$ on the basis of a lack of measurement capability on JET, or in the case of edge T_i charge-exchange recombination spectroscopy measurements, difficulties in interpretation of the data near the separatrix. For the L-mode dataset we use the multi-machine L-mode λ_q scaling from [32].

(b) In the detailed treatment, ‘rev-2PM-detailed’, we adopt the modified $\lambda_q(\alpha_t)$ scaling from AUG and infer τ_t, τ_u and f_{conv} from the simulations as approximate functions of $\langle T_{e,\text{ot}} \rangle$. The EDGE2D fluid model accounts for thermal equipartition power between ions and electrons and includes kinetic corrections via heat flux limit factors [33], which have been found to be necessary to match experimental data, for example on Alcator C-Mod, in which detailed measurements of the ion–electron temperature ratio were assessed [34].

Lastly, when utilizing 2PM formatting of edge simulation output, the model is typically applied to individual flux tubes to relate the spatially resolved radial profiles of the upstream driver and target parameters, and thus implicitly assuming that recycled neutrals on each flux tube are ionized on the same flux tube [3]. Moreover, the first SOL flux tube next to the separatrix is usually ignored due to an additional particle, momentum and energy sink associated with cross-field transport into the private flux region. Due to the challenges associated with obtaining flux tube resolved upstream and target measurements from experiment for the range of divertor configurations considered, we instead apply equation (3) to relate $n_{e,\text{sep}}$ to $\langle T_{e,\text{ot}} \rangle$ in section 5 with the expectation that a leading coefficient will be needed to match the measurements as this approach deviates from the way in which the 2PM is typically applied. This same approach is utilized in interpreting the modelling results to maintain consistency between experiment and code comparisons.

4. Volumetric pressure-momentum and cooling losses in the SOL-divertor

From the divertor perspective, the optimal target plasma conditions required for viable divertor operation in DT tokamaks with solid plasma facing components (PFCs) are established based on requirements for (a) maintaining the steady-state deposited peak heat flux below acceptable levels, typically quoted as $q_{\perp,\text{peak}} = 10 \text{ MW m}^{-2}$ (e.g. [11]); and (b) suppressing the net erosion of the solid target to prevent a rapid loss of material and thus ensure material survivability over the lifetime of a high duty cycle reactor [3]. Satisfying these constraints leads to divertor plasma conditions requirements of $T_{e,t} < 5\text{--}10 \text{ eV}$, $n_{e,t} \sim 10^{21} \text{ m}^{-3}$. Driving down $T_{e,t}$ from values approaching the upstream separatrix temperature ($T_{e,\text{sep}} \sim 100\text{--}200 \text{ eV}$ depending on the power crossing the separatrix) to below 10 eV can be achieved by increasing the fuel species particle inventory in the SOL to promote high-recycling and volumetric power and momentum losses via neutral-plasma interactions, as well as introducing extrinsic impurities to dissipate the majority of the exhaust power isotropically via line radiation. Restricting the present discussion to loss channels via neutral-plasma interactions (see e.g. [35] for a more detailed description of the atomic and molecular processes involved), a primary dependence of the volumetric momentum and power losses on $T_{e,t}$ emerges based on the analysis of multi-machine 2D edge plasma simulations

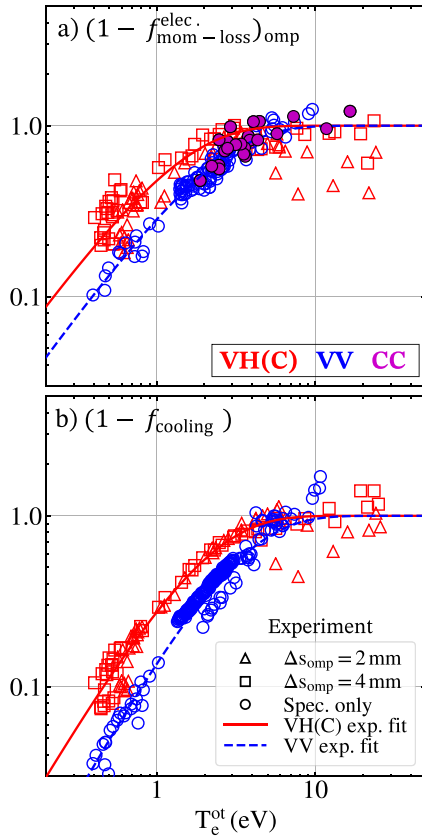


Figure 2. $(1 - f_{\text{mom-loss}})$ and $(1 - f_{\text{cooling}})$ estimates from L-mode density ramps in VH(C), VV and CC.

[3], and supported by observations from experiments [36, 37]. Hence, whereas the main actuators are the auxiliary heating power and gas puffing rate, $T_{e,t}$ is the basic physics parameter which strongly correlates with the volumetric energy and momentum loss factor trends, which in turn are needed to relate the ‘upstream’ and ‘downstream’ quantities in the 2PM in dissipative divertor regimes.

The volumetric pressure loss, $(1 - f_{\text{mom-loss}})$ and cooling loss $(1 - f_{\text{cooling}})$ factors were estimated in L-mode density ramp discharges for the VH(C), VV configurations, and partially for the CC configuration, according to equations (1), (2), and (5), as shown in figure 2. Flux tube resolved $T_{e,t}$ estimates were obtained in the VH(C) configuration away from the unresolved peak $T_{e,t}$ near the separatrix by applying a correction factor to the spatially resolved Langmuir probe (LP) $T_{e,t}$ measurements (see figure 2 in [1]) using the spectroscopically measured value of $\langle T_{e,ot} \rangle$. The spatially resolved results are approximately mapped to the distance from the separatrix at the OMP, Δs_{omp} . Further details on the empirical correction for the kinetic distortion effects impacting the LP $T_{e,t}$ and $n_{e,t}$ target profiles are given in [38]. In the VV and CC configurations, only the averaged spectroscopic $\langle T_{e,ot} \rangle$ values were used due to a lack of spatially resolved measurements.

HRTS $T_{e,u}$ and $n_{e,u}$ radial profiles [14] in the edge plasma near the separatrix position were used to estimate the upstream electron static pressure. 2D tomographic reconstructions from resistive bolometer cameras [39] were used to estimate $P_{\text{rad-core}}$

and hence $P_{\text{SOL}} = P_{\text{Ohm}} + P_{\text{NBI}} - P_{\text{rad-core}}$, whereas the L-mode power width scaling from [32] (the ‘F2’ multi-machine scaling) was used to account for the observed λ_q widening with increasing density (decreasing $\langle T_{e,ot} \rangle$), giving $\lambda_q \propto f_{\text{GW}}^{0.9}$ for fixed machine parameters, where f_{GW} is the Greenwald density limit fraction [40]. Uncertainties in P_{SOL} and hence $q_{\parallel u}$ and inner–outer power sharing asymmetries were addressed with the assumption that at low recycling conditions, $(1 - f_{\text{cooling}}) \approx 1$, as the volumetric power loss in the SOL is expected to be small. Similarly, uncertainties in the position of the last closed-flux surface (LCFS) in the radial $T_{e,u}$ and $n_{e,u}$ profiles combined with the absence of upstream fuel ion parallel fluid velocity and $T_{i,u}$ measurements are addressed by assuming $M_u = 0$ and $T_i = T_e$ such that $p_{\text{tot},u} \approx 2n_{e,u}kT_{e,u}$ and $p_{\text{tot},t} \approx 4n_{e,t}kT_{e,t}$ with $M_t = 1$ (i.e. the basic form of the Bohm–Chodura sheath condition). Thus the measured electron pressure-momentum losses are assumed to approximate the total pressure-momentum losses, $(1 - f_{\text{mom-loss,elec}}) \approx (1 - f_{\text{mom-loss}})$, and $(1 - f_{\text{mom-loss}}) \approx 1$ in low recycling conditions. The validity of these assumptions is discussed below based on flux tube resolved comparisons of $(1 - f_{\text{mom-loss}})$ from EDGE2D density scans shown in figure 3 using the total (static + dynamic) upstream pressure, and electron pressure, with the upstream locations taken at the X-point as well as at the OMP.

The main observation from the experiment results (figure 2) is that the onset of electron pressure-momentum losses occurs at about 3–4 eV for all three divertor configurations, within the limitations of mapping $(1 - f_{\text{mom-loss,elec}})$ to $\langle T_{e,ot} \rangle$ for the CC and VV configurations. Below 3 eV, the VV $(1 - f_{\text{mom-loss,elec}})$ trend exhibits a steeper fall-off relative to VH(C), while for the CC configuration there are insufficient data points below 3 eV to resolve the pressure losses.

The $(1 - f_{\text{mom-loss,elec}})$ experiment trends are in best agreement with the EDGE2D L-mode-like total pressure trends with the upstream position taken at the X-point, $(1 - f_{\text{mom-loss,tot}})_{\text{Xpt}}$, shown in figure 3(a), with similar differences observed between VH(C) and VV configurations. Changing the upstream location from the X-point to the OMP in formatting the EDGE2D output gives only a small increase in $(1 - f_{\text{mom-loss,tot}})_{\text{omp}}$ (figure 3(b)), and can be attributed to the divertor configuration influence on poloidal ionization and density distributions, as discussed in section 6.2. However, significant changes to the pressure loss trends are obtained if only the electron pressure is considered, as shown in figures 3(c) and (d). The influence of T_i on the upstream and target total pressure is further clarified in figure 4, which shows τ_u and τ_t as a function of $T_{e,t}$. At high $T_{e,t}$, $T_i > T_e$ upstream, while $T_i < T_e$ at the target. As collisionality in the SOL increases and $T_{e,t}$ decreases, $T_{e,t}$ and $T_{i,t}$ equilibrate, with τ_t reaching unity at 3 eV while τ_u decreases from about 2–1.5 at low $T_{e,t}$.

A discrepancy between the experiment and EDGE2D $(1 - f_{\text{mom-loss,elec}})$ results is therefore apparent, since a constant τ_u and τ_t is assumed in experiment by necessity due to a lack of information on the ion temperature in the SOL, yet the observed trends are more consistent with the EDGE2D $(1 - f_{\text{mom-loss,tot}})$ trends using total pressure, rather than electron pressure. It is possible that the influence of electron and

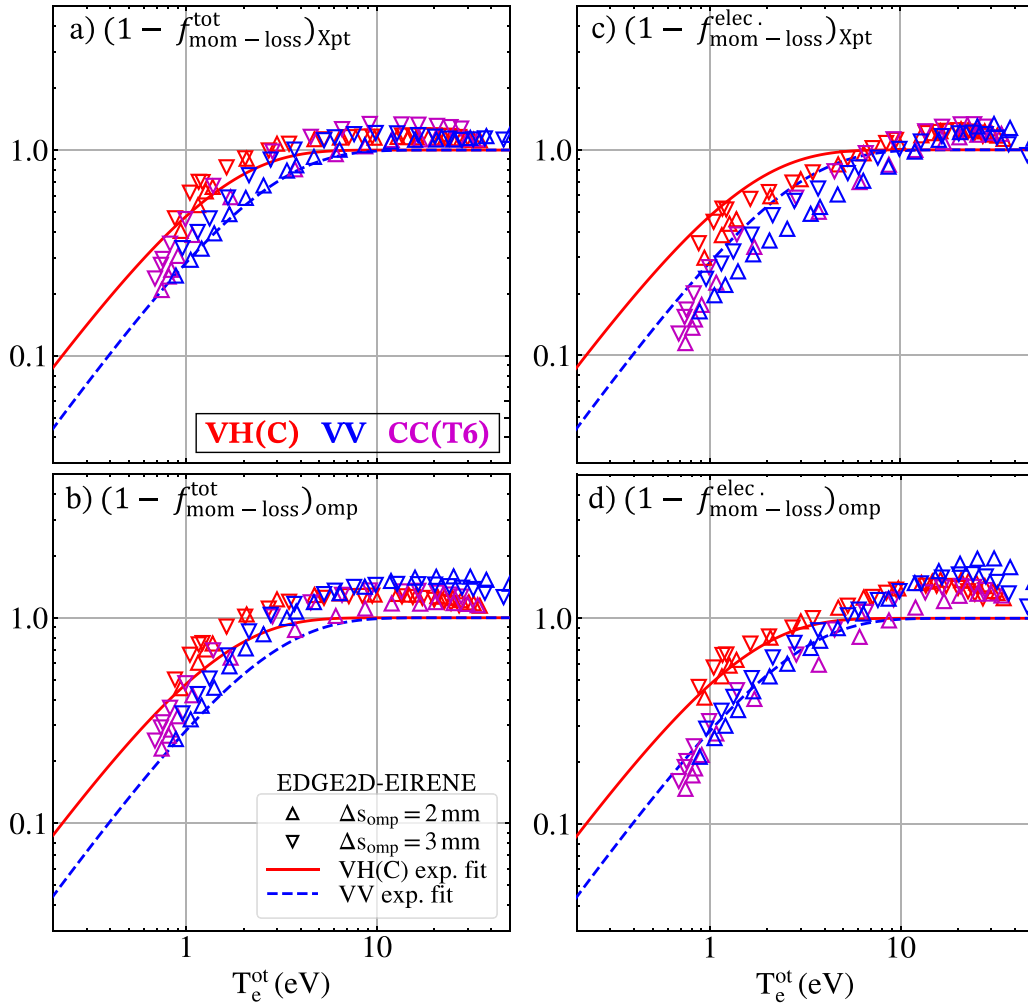


Figure 3. Total and electron pressure loss factors derived from EDGE2D-EIRENE L-mode-like simulations with the upstream location taken at the X-point (a), (c) and outer midplane (b), (d).

ion temperature equilibration on the pressure loss trends is obscured by reduced sensitivity in the $n_{e,t}$ and $T_{e,t}$ spectroscopic measurements in low recycling conditions, since the quality of these measurements improves at higher $n_{e,t}$ and lower $T_{e,t}$. Further constraints on T_i from experiment are required to make more definitive statements regarding this discrepancy. Activation of drifts in the L-mode-like EDGE2D density VH(C) and VV scans has only a minor impact on the above trends.

In figure 5(a) the EDGE2D VH(C) and VV momentum losses are interpreted in a manner consistent with the analysis in experiment: flux tube resolved measurements of $(1 - f_{\text{mom-loss,elec}})$ for the diagnostically optimized VH(C) geometry, while mapping $(1 - f_{\text{mom-loss,elec}})$ to $\langle T_{e,ot} \rangle$ for the VV configuration with the upstream location at the OMP, with the assumption $p_{\text{tot,u}} \approx 2n_{e,u}kT_{e,u}$ and $p_{\text{tot,t}} \approx 4n_{e,t}kT_{e,t}$. The trends have been normalized to the values at 10 eV for consistency with the experiment trends in figure 2 and the assumption that $(1 - f_{\text{mom-loss,elec}}) \approx 1$ in low recycling conditions. Good agreement is still obtained between the experiment and EDGE2D $(1 - f_{\text{mom-loss,elec}})$ trends for the VV configuration, giving

confidence in mapping the results to $\langle T_{e,ot} \rangle$ in the absence of spatially resolved $T_{e,t}$ measurements. The moderately steeper slope for the VV configuration at low $\langle T_{e,ot} \rangle$ persists regardless of the interpretation approach.

Considering next the experiment $(1 - f_{\text{cooling}})$ trends shown in figure 2(b), these estimates are based on flux tube resolved $T_{e,ot}$ measurements for the VH(C) configuration, whereas $\langle T_{e,ot} \rangle$ is used for the VV configuration, consistent with the $(1 - f_{\text{mom-loss,elec}})$ interpretation. The results are normalized to $(1 - f_{\text{cooling}}) = 1$ at 10 eV due to uncertainty in P_{sol} and the position of the LCFS. The $(1 - f_{\text{cooling}})$ results show that the onset of volumetric cooling losses occurs at around 10 eV, and, similar to the $(1 - f_{\text{mom-loss,elec}})$ results, a steeper slope/fall-off is observed in the VV configuration below 5 eV. Cooling loss estimates for the CC configuration were not possible due to insufficient information on $n_{e,t}$ and lack of data at low $T_{e,ot}$. The observed differences between VH(C) and VV are reproduced in the EDGE2D L-mode-like density scans, as shown in figure 6, if the results are formatted from the simulation output according to equation (2). Values of $(1 - f_{\text{cooling}})_{\text{omp}} > 1$ in the EDGE2D results reflect the fact that q_{\parallel} is not divergence

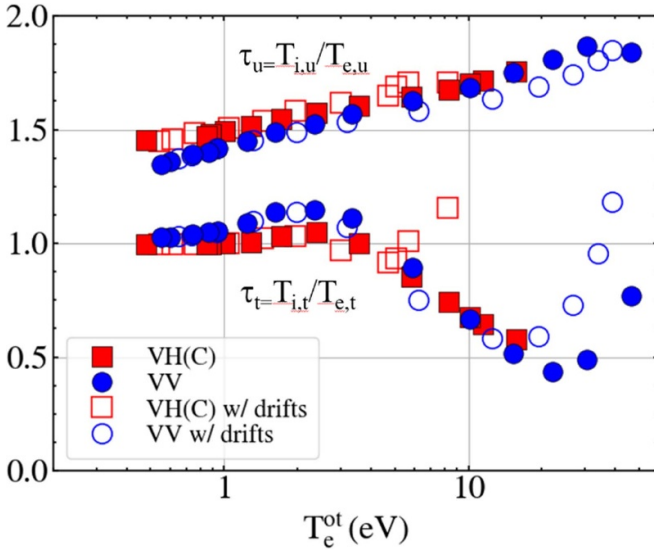


Figure 4. VH(C) and VV $\tau_u = T_{i,u}/T_{e,u}$ and $\tau_t = T_{i,t}/T_{e,t}$ trends from EDGE2D L-mode-like density scan simulations with shown values corresponding to the third SOL flux tube from the separatrix ($\Delta s_{omp} = 2$ mm) and upstream location taken at the outer midplane.

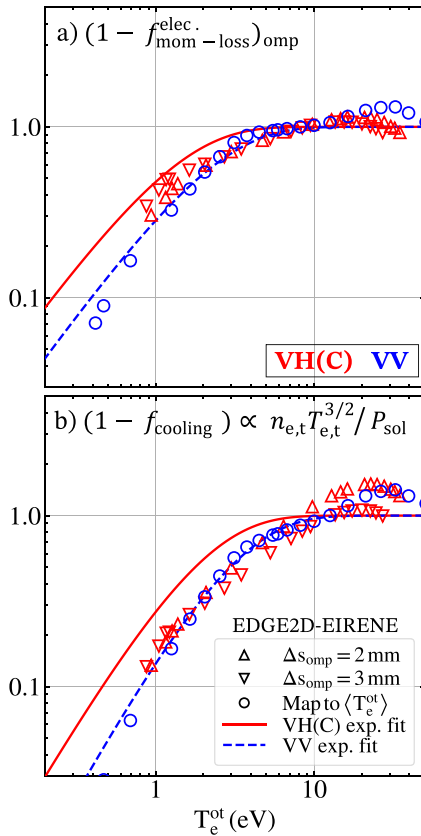


Figure 5. EDGE2D L-mode-like momentum and cooling loss factors consistent with interpretation of experiment data shown in figure 2.

free between the OMP and the X-point. More specifically, the EDGE2D $(1 - f_{cooling})_{omp}$ trends are in better agreement with the best fit lines obtained from experiment, if these are

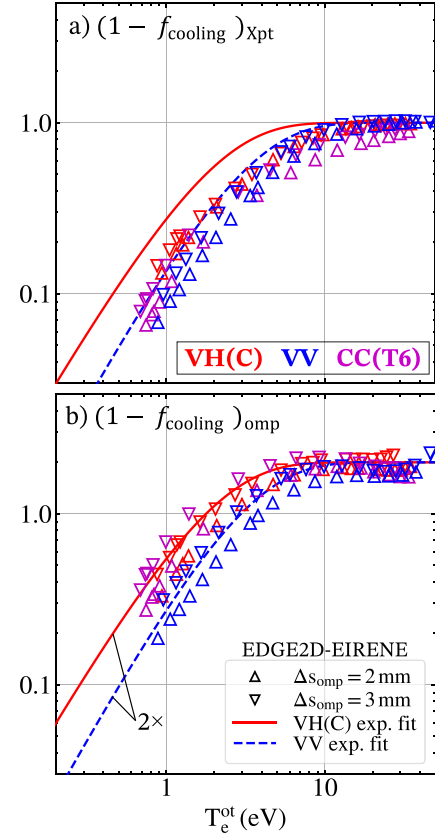


Figure 6. Comparison of EDGE2D L-mode-like cooling loss factors with the upstream location taken at the X-point (a) and outer midplane (b).

scaled by a factor of 2. Hence, normalizing the EDGE2D $(1 - f_{cooling})_{omp}$ data in the same manner as the estimates from experiments, such that $(1 - f_{cooling})_{omp} = 1$ at high $T_{e,ot}$, leads to good agreement with the experiment trends. If the cooling losses are calculated taking the upstream position at the X-point instead (figure 6(a)), the EDGE2D trends are observed to be somewhat steeper compared to the experiment.

Lastly, figure 5(b) shows cooling losses from the simulation results which are post-processed in a manner consistent with the interpretation of the experiment data (i.e. $(1 - f_{cooling}) \propto T_{e,t} \Gamma_{||} / P_{sol} \propto n_{e,t} T_{e,t}^{3/2} P_{sol}^{-1}$, assuming $(1 - f_{cooling}) = 1$ at 10 eV and mapping the VV configuration results to $\langle T_{e,ot} \rangle$ due to lack of spatially resolved $T_{e,t}$ measurements). In these estimates, the VH(C) trend is steeper compared to the experiment fit as well as the actual EDGE2D output calculated using equation (3) with the upstream location at the OMP (figure 6(b)). The difference between the VH(C) and VV trends in figure 5(b) is thus diminished.

From the above interpretations and code formatting, it is clear that the lack of more complete information from experiment required for evaluating the volumetric pressure-momentum and cooling losses poses a challenge in undertaking meaningful comparisons of the observed trends with simulation results. The selection of upstream location, assumptions on τ_u and τ_t , and the limitations of the $T_{e,ot}$ spatial resolution all contribute to modifying the $(1 - f_{mom-loss})$ and

$(1 - f_{\text{cooling}})$ trends, depending on the interpretation approach. Nevertheless, in most of the comparisons above, the steeper slope in the VV geometry is a consistent feature, and is likely attributed to differences in the recycling and ionization patterns and neutral pathways in the vertical target geometry, as discussed in section 5.2 based on a detailed numerical study on this effect [41]. The key point is that the basic functional form and primary $T_{e,\text{ot}}$ dependence of the $(1 - f_{\text{cooling}})$ and $(1 - f_{\text{mom-loss}})$ loss factors, and their role in evolving $n_{e,\text{sep}}$ according to the rev-2PM formulation (equation (3)), relies on accurate measurement of several upstream and target quantities, as discussed above, in order to capture the influence of the $(1 - f_{\text{cooling}})/(1 - f_{\text{mom-loss}})$ ratio on $n_{e,\text{sep}}$.

5. 2PM $n_{e,\text{sep}}$ estimates in experiment and EDGE2D simulations

5.1. 'rev-2PM-simplified' $n_{e,\text{sep}}$ estimates—H-mode dataset

Figure 7(a) shows a comparison between the measured $n_{e,\text{sep}}$ results spanning the entire H-mode dataset and $n_{e,\text{sep}}$ estimates recovered using equation (3) assuming the rev-2PM-simplified treatment (i.e. $\lambda_q \propto B_p^{-1}$ estimated using the ITPA H-mode scaling, constant $T_{e,\text{sep}}$, $\tau_t = \tau_u = 1$, $f_{\text{conv}} = 0$, and hence the separatrix location, estimated using equation (4)). The rev-2PM-simplified model recovers the measured $n_{e,\text{sep}}$ values reasonably well if a scaling factor of 0.2 is used to account for the use of an averaged target temperature $\langle T_{e,\text{ot}} \rangle$ rather than resolving the measurements on an individual flux tube basis, giving $a \pm 25\%$ uncertainty range with no clear divertor configuration dependence observed within the scatter of the data.

Applying the same interpretation approach to EDGE2D H-mode-like density scans (i.e. using equation (4) to obtain $T_{e,\text{sep}}$ and $n_{e,\text{sep}}$, and the rev-2PM-simplified model to format the simulation output) the comparison between the 'measured' and rev-2PM-simplified $n_{e,\text{sep}}$ is shown in figure 7(b), with a scaling factor of 0.3 applied to the rev-2PM-simplified results. There is typically $< 10\%$ difference in the EDGE2D results between the actual OMP $n_{e,\text{sep}}$ and the value obtained at the position of $T_{e,\text{sep}}$ evaluated using equation (4) (typically around 100 eV) since the OMP radial n_e and T_e experiment profiles used to constrain the radial transport coefficients are already shifted to $T_{e,\text{sep}} \approx 100$ eV, which is a reasonable value representative of JET H-mode scenarios. Similar to the experiment results, the rev-2PM-simplified $n_{e,\text{sep}}$ values are consistently within $\pm 15\%$ of the 'measured' values over the range of density scans for the VV and VH(C) configurations, with only a modest difference between the two divertor configurations. Furthermore, the comparable values of the rev-2PM-simplified scaling factors needed to align the linear trends to the experimental results (0.2 in experiment, 0.3 in EDGE2D) reinforce the validity of applying the 2PM in the non-conventional manner by using the target quantity $\langle T_{e,\text{ot}} \rangle$ instead of the flux tube resolved $T_{e,t}$.

In formatting the EDGE2D results, there is a moderate sensitivity of the trends in figure 7(b) to the weighting parameter used in averaging the electron temperature over the outer target, $T_{e,\text{ot}} = \int w(s) T_{e,t}(s) ds / \int w(s) ds$, where s is the

distance along the outer target in the common SOL from the OSP outward, and $w(s)$ is either $n_{e,t}$, $n_{e,t}^2$ or j_{sat} . Weighting $T_{e,t}$ by the particle flux or target density approximates the line-integrated spectroscopic measurements, which are weighted by the brightness of the Balmer photo-recombination continuum volumetric emission $\propto n_e^2$. For simplicity we use $j_{\text{sat}}(s)$ as the weighting parameter in formatting all of the simulation output, recognizing that while the interpretation of $\langle T_{e,\text{ot}} \rangle$ as a basis for comparing the experiment data to simulations is not straightforward, consistency in interpreting $\langle T_{e,\text{ot}} \rangle$ is more important than the choice of weighting parameter.

The importance of the volumetric loss terms on the rev-2PM-simplified $n_{e,\text{sep}}$ estimates is also illustrated in figure 7, where $n_{e,\text{sep}}$ is evaluated with and without the $(1 - f_{\text{mom-loss}})$ and $(1 - f_{\text{cooling}})$ terms, i.e. by setting $f_{\text{mom-loss}} = f_{\text{cooling}} = 0$. In doing so, a divergence away from the linear trend is observed at high $n_{e,\text{sep}}$, with $\langle T_{e,\text{ot}} \rangle < 10$ eV, corresponding to the onset of cooling losses. With the $(1 - f_{\text{mom-loss}})$ and $(1 - f_{\text{cooling}})$ terms included, the radiative and ionization-dissociation energy losses associated with the $(1 - f_{\text{cooling}})$ term outweigh the momentum losses at low $\langle T_{e,\text{ot}} \rangle$ (see figure 2). Thus, despite a further decrease in $(1 - f_{\text{mom-loss}})$ when $\langle T_{e,\text{ot}} \rangle$ is driven down by additional gas fueling, the rise in $n_{e,\text{sep}} \propto \langle T_{e,\text{ot}} \rangle^{-1/2} [(1 - f_{\text{cooling}})/(1 - f_{\text{mom-loss}})]$ is suppressed at low $\langle T_{e,\text{ot}} \rangle$ by the steeper $(1 - f_{\text{cooling}})$ trend.

Since the $\langle T_{e,\text{ot}} \rangle^{-1/2}$ term in equation (3) dominates over $[(1 - f_{\text{cooling}})/(1 - f_{\text{mom-loss}})]$ when $\langle T_{e,\text{ot}} \rangle > 10$ eV, we can attribute the pronounced reduction in $H_{98(y,2)}$ with rising $n_{e,\text{sep}}$ and decreasing $\langle T_{e,\text{ot}} \rangle$ from 30 to 10 eV shown in [1] mainly to parallel pressure balance as the target pressure, $p_{\text{tot,t}} \approx 4n_{e,t}kT_{e,t}$, and recycling particle flux increase with additional D₂ fueling. Below 10 eV, the $(1 - f_{\text{cooling}})/(1 - f_{\text{mom-loss}})$ ratio in equation (3) plays a more important role in linking divertor detachment with the upstream $n_{e,\text{sep}}$, and, to the extent that neutrals penetrate into the confined plasma in low opacity edge plasma conditions, the pedestal density, $n_{e,\text{ped}}$. All of the H-mode discharges in the dataset remain below the H-mode density limit, with additional D₂ fueling required to reach the limit being constrained in JET-ILW by neutral beam reionization hot spots on limiter PFCs occurring in discharges with moderate-to-high neutral beam heating power.

As an aside, suppressing $n_{e,\text{sep}}$ at low $\langle T_{e,\text{ot}} \rangle$ in order to minimize pedestal collisionality requires more pronounced $(1 - f_{\text{cooling}})$ losses with a higher $\langle T_{e,\text{ot}} \rangle$ onset. This can be achieved by promoting radiative dissipation in the divertor with extrinsic impurity seeding such that $f_{\text{cooling}} \approx f_{\text{rad,imp}}$. However, since both power and momentum loss channels are important, the influence of extrinsic impurity seeding on the variation in the $(1 - f_{\text{cooling}})/(1 - f_{\text{mom-loss}})$ ratio has not been demonstrated. So far, a surprisingly strong correlation between $(1 - f_{\text{cooling}})$ and $(1 - f_{\text{mom-loss}})$ has been observed from edge plasma simulation datasets compiled by Stangeby [3] for scans that include extrinsic seeded impurities. It remains to be seen whether this correlation can be broken, as is the expectation, given that $(1 - f_{\text{cooling}})$ is in principle freely specifiable with power losses being more spatially distributed over the divertor and SOL whereas momentum losses largely occur in a small region in front of the divertor target.

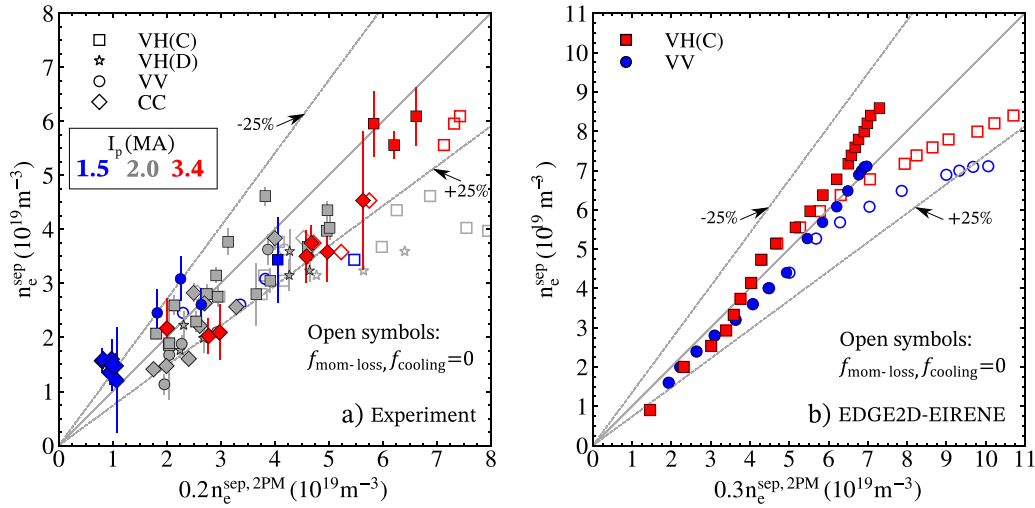


Figure 7. Comparison of measured $n_{e,sep}$ with estimates using the *rev-2PM-simplified* model for the entire H-mode dataset from experiment (a) and the EDGE2D H-mode-like density scans (b). Open symbols correspond to *rev-2PM-simplified* $n_{e,sep}$ estimates in which the momentum and cooling loss factors have been neglected. In (b) the ‘measured’ $n_{e,sep}$ is estimated using the location along the radial profile corresponding to $T_{e,sep}$ calculated with equation (4) for consistency with experiment.

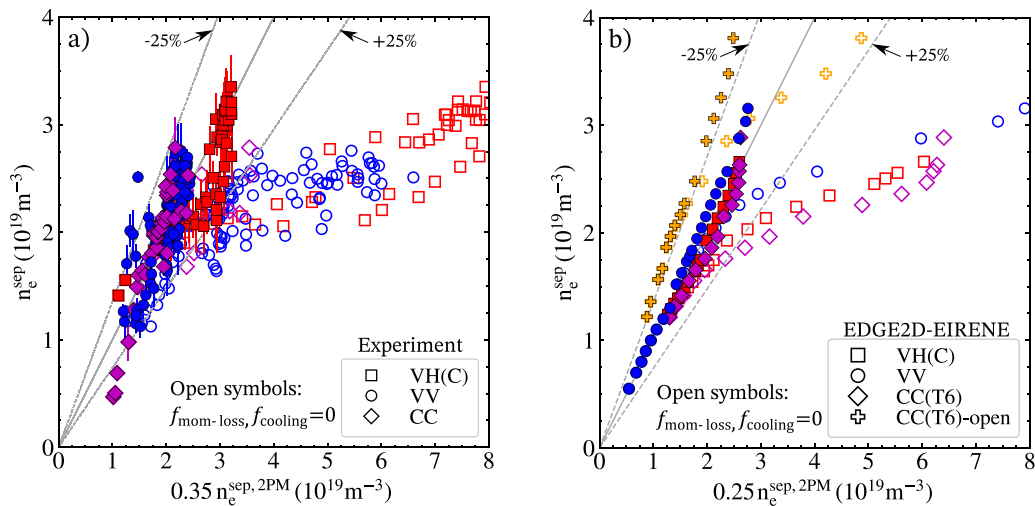


Figure 8. Comparison of measured $n_{e,sep}$ with estimates using the *rev-2PM-simplified* model for the L-mode dataset from experiment (a) and the EDGE2D L-mode-like density scans (b). Open symbols correspond to *rev-2PM-simplified* $n_{e,sep}$ estimates in which the momentum and cooling loss factors have been neglected.

5.2. ‘*rev-2PM-simplified*’ $n_{e,sep}$ estimates—L-mode dataset

Applying the *rev-2PM-simplified* treatment to recover $n_{e,sep}$ from the L-mode density ramp discharges and EDGE2D L-mode-like density scan datasets shown in figure 8 yields approximately similar trends to the H-mode results. Despite moderate scatter and non-linearity in the experiment data, especially for the VH(C) configuration in figure 8(a), the measured $n_{e,sep}$ values are recovered to within $\pm 25\%$, with modifications to the leading coefficient to align the trends (0.35 in experiment, 0.25 in EDGE2D). Since the ITPA λ_q scaling from [30] was derived from a multi-machine regression of H-mode data, its applicability to the L-mode data is in question. Substituting the F2 L-mode scaling, $\lambda_q \propto B_\phi^{-0.2} q_{95}^{0.52} f_{GW}^{0.9}$, from [32] has only a modest impact

on the trends given the small range in I_p (2–2.5 MA) in the L-mode density ramps, and relatively weak λ_q dependence on f_{GW} . Hence, for the limited L-mode dataset, the choice of λ_q scaling did not significantly change the results.

Despite the high quality measurements of the $(1 - f_{cooling})$ and $(1 - f_{mom-loss})$ factors for the VH(C) configuration, better agreement to the measured $n_{e,sep}$ in experiment was obtained for the VH(C) configuration in figure 8(a) by using the VV $(1 - f_{cooling})$ and $(1 - f_{mom-loss})$ fit coefficients. However, the selection of either the VH(C) or the VV $(1 - f_{cooling})$ and $(1 - f_{mom-loss})$ fit coefficients has only a moderate impact on the results compared to the *rev-2PM-simplified* $n_{e,sep}$ estimates for which the $(1 - f_{cooling})$ and $(1 - f_{mom-loss})$ factors are neglected altogether, as also shown in figure 8. The impact of these loss terms is clearly more pronounced in

the L-mode dataset as the density ramps are not limited by neutral beam reionization hot spots, and can be extended to deep detachment past the outer target ion current rollover point down to very low $\langle T_{e,ot} \rangle = 0.5$ eV (see figure 3 in [1]), by which point the $(1 - f_{cooling})$ and $(1 - f_{mom-loss})$ factors have decreased by an order of magnitude or more. In this low temperature, pronounced particle detachment regime, the $(1 - f_{cooling})/(1 - f_{mom-loss})$ ratio is clearly the dominant term suppressing a further rise in $n_{e,sep}$. The relatively linear trends obtained when the volumetric loss terms are included reinforces the fact that the $(1 - f_{cooling})$ and $(1 - f_{mom-loss})$ estimates are essential for reconciling the measured $n_{e,sep}$, despite the discrepancies within the $\pm 25\%$ data scatter.

For consistency with the interpretation of experiment data, all of the EDGE2D *rev-2PM-simplified* results in figure 8(b) were also evaluated using the VV $(1 - f_{cooling})$ and $(1 - f_{mom-loss})$ fit coefficients obtained from experiment, although, as already mentioned above, the choice of fit coefficients from either the VV or VH(C) $(1 - f_{cooling})$ and $(1 - f_{mom-loss})$ trends mainly shifts the $n_{e,sep,2PM}$ scaling factor without much influence on the overall trends. The EDGE2D results also include the CC(T6)-open configuration, which corresponds to the wide open divertor geometry with the outer divertor baffles entirely removed. Whereas the differences between the VH(C), VV and CC(T6) $n_{e,sep,2PM}$ EDGE2D trends are relatively small, a markedly steeper trend is obtained for the CC(T6)-open configuration using the same value for the leading coefficient. This steeper trend arises because the same leading coefficient is no longer valid for the hypothetical wide open configuration due to considerably higher neutral leakage and higher $n_{e,sep}$, as will be shown in section 6. These effects are captured in the 2PM as an increase in the $(1 - f_{cooling})/(1 - f_{mom-loss})$ ratio when taken at the OMP, mainly caused by a downward vertical shift in the $(1 - f_{mom-loss}) \propto n_{e,sep}^{-1}$ trend at high $\langle T_{e,ot} \rangle$ above the momentum loss onset temperature. Combined with a roughly 15% increase in $\tau_u = T_{iu}/T_{eu}$ in the CC(T6)-open configuration due to higher ionization levels at the OMP, an overall correction factor of about 1.5 is obtained in order to align the CC(T6)-open *rev-2PM-simplified* $n_{e,sep}$ results in figure 8(b) onto the 1:1 trend line.

The above results indicate that: (a) the variation in the VV, VH(C) and CC(T6) divertor configurations (including closure and target inclination) is not sufficient to cause significant differences in the $(1 - f_{cooling})/(1 - f_{mom-loss})$ ratio; and (b) generalizing the *rev-2PM* to capture large changes in geometry relies on detailed 2D modelling since variations in neutral dynamics and their influence on upstream conditions are encoded in the $(1 - f_{cooling})/(1 - f_{mom-loss})$ ratio, τ_u , as well as τ_t , and f_{conv} , which are discussed next.

5.3. Capturing additional physics processes with the 'rev-2PM-detailed' model-based approach

The measured $n_{e,sep}$ in both experiment and EDGE2D simulations can be recovered using the *rev-2PM-simplified* treatment reasonably well, despite the fairly simplistic assumptions on $\lambda_q \propto B_p^{-1}$ estimated from the ITPA H-mode scaling in

attached conditions, neglecting the convective fraction of the parallel heat flux $q_{lu,conv} = f_{conv} q_{lu}$, and neglecting the τ_u , and τ_t dependence on collisionality. The details of neutral leakage, ionization distributions, modifications to cross-field transport in the SOL and λ_q widening with increasing collisionality are encoded in these terms and the $(1 - f_{cooling})/(1 - f_{mom-loss})$ ratio.

With the *rev-2PM-detailed* treatment, we attempt to quantify the influence of these additional terms on recovering the measured $n_{e,sep}$ values by utilizing the more recent $\lambda_q(\alpha_i)$ scaling accounting for power width widening, and employing the EDGE2D density scans to *approximate* τ_u , and τ_t due to the lack of $T_{i,t}$ and $T_{i,u}$ measurements in experiment, as well the convective parallel heat flux contribution. We focus on the L-mode-like EDGE2D density scans from [16, 17] in VV ($P_{in} = 2.8$ MW) and VH(C) ($P_{in} = 3.8$ MW) configurations, since the plasma solutions in these scans were successfully converged with the drift terms activated, allowing a direct comparison of the influence of drifts and the additional terms in the *rev-2PM-detailed* treatment. Given the primary dependence of $(1 - f_{mom-loss})$ and $(1 - f_{cooling})$ and $n_{e,sep} \propto T_{e,t}^{-1/2} [(1 - f_{mom-loss})/(1 - f_{cooling})]$ on $T_{e,t}$ in unseeded deuterium plasmas, we expect the observations from L-mode trends to be applicable to unseeded H-mode plasmas. However, the presence of ELMs in H-modes will likely introduce additional dynamics (e.g. fuel species implantation and desorption on W PFCs [42]) superimposed on the inter-ELM steady-state behavior, and a stronger cross-field $E_\theta \times \mathbf{B}$ drift drive due to higher $T_{e,sep}$ approximated by equation (4), since $E_\theta \propto dT/ds$, where E_θ is the poloidal electric field and s is the poloidal distance in the SOL.

Figure 9(a) shows the convective heat flux term $(1 - f_{conv})$ from the EDGE2D L-mode-like VV and VH(C) density scans evaluated at the OMP in the flux tube adjacent to the separatrix. At $\langle T_{e,ot} \rangle > 10$ eV, with low collisionality in the SOL and the divertor near the sheath-limited regime (small poloidal ∇T_e), convection dominates the upstream SOL parallel heat flow. Activation of drifts further enhances the convective contribution, especially for the VH(C) configuration, with $(1 - f_{conv}) < 0.35$ at $\langle T_{e,ot} \rangle \approx 10$ eV. At $\langle T_{e,ot} \rangle < 10$ eV, parallel electron conduction overtakes convection as the dominant heat flow mechanism, leading to $(1 - f_{conv}) > 0.75$ in the cases without drifts, while a larger convective contribution persists for the cases with drifts. Substituting the $(1 - f_{conv})$ values into equations (3) and (4) yields the *rev-2PM* results shown in figure 9(c), which overestimate $n_{e,sep}$ compared to the *rev-2PM-simplified* results shown in figure 9(b). This is most pronounced for the VH(C) configuration at low densities and with drifts activated, corresponding to the lowest $(1 - f_{conv})$ values. Interestingly, further substitution of τ_u and τ_t values shown in figure 9(d) improves the 2PM $n_{e,sep}$ agreement, except for the lowest $n_{e,sep}$ cases with drifts in the VH(C) configuration. These results suggest that the $(1 - f_{conv})$ term is, to a large extent, balanced by the τ_u and τ_t terms in equation (3), at least for the examined cases. It is not clear how general this result is, since there is a configuration dependence on $(1 - f_{conv})$ with the VV results in figures 9(b)–(d) being less sensitive to the assumptions on f_{conv} , τ_u and τ_t .

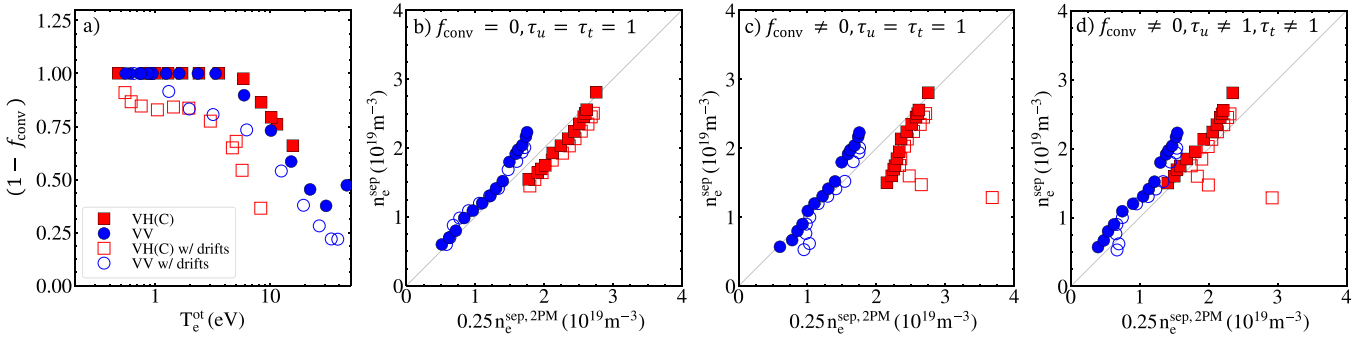


Figure 9. (a) EDGE2D convective fraction as a function of the outer target electron temperature in the third SOL flux tube from the separatrix ($\Delta s_{\text{comp}} = 2$ mm) with the upstream location taken at the outer midplane; (b) rev-2PM $n_{e,\text{sep}}$ estimates assuming $f_{\text{conv}} = 0$, $\tau_u = \tau_t = 1$; (c) $f_{\text{conv}} \neq 0$, $\tau_u = \tau_t = 1$ and (d) $f_{\text{conv}} \neq 0$, $\tau_u \neq 1$, $\tau_t \neq 1$ with and without drifts.

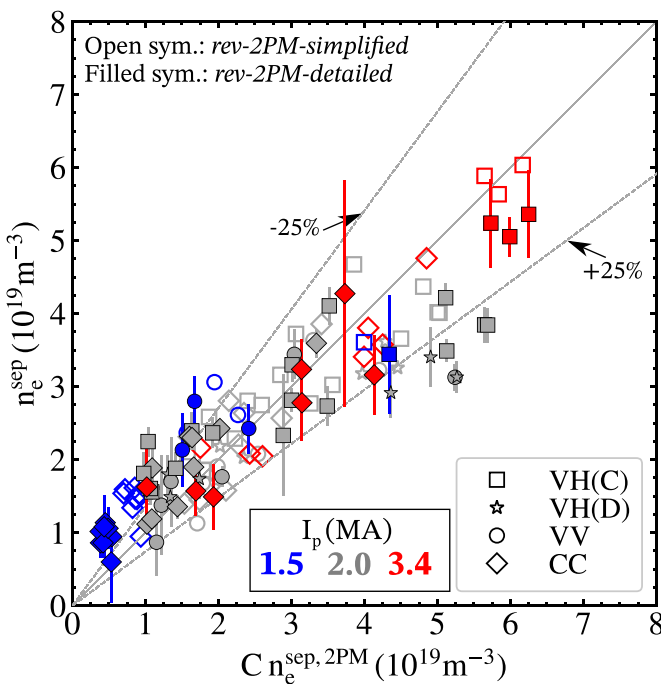


Figure 10. Comparison of measured $n_{e,\text{sep}}$ with estimates using the *rev-2PM-simplified* model (open symbols, $C = 0.2$) and *rev-2PM-detailed* model (filled symbols, $C = 0.3$) for the entire H-mode dataset.

An important oversimplification in the above is the assumption of fixed cross-field transport coefficients for the entire range of the density scans. Varying the diffusive radial transport coefficients in a self-consistent manner as a function of collisionality, as was demonstrated in [25], for example, may also influence the $(1 - f_{\text{conv}})$, τ_u and τ_t trends, and this needs to be further clarified. We nevertheless proceed to apply the EDGE2D $(1 - f_{\text{conv}})$, τ_u and τ_t estimates as functions of $\langle T_{e,\text{ot}} \rangle$ to the H-mode experimental dataset, in addition to replacing the ITPA λ_q scaling with the more recent $\lambda_q(\alpha_t)$ scaling from AUG to resolve the power width widening. The comparison of the *rev-2PM-simplified* and *rev-2PM-detailed* H-mode $n_{e,\text{sep}}$ results is shown in figure 10. The observed decrease in the $n_{e,\text{sep}}$ values estimated with the *rev-2PM-detailed* model is mainly attributed to the influence of the convective fraction

on the separatrix temperature and therefore the separatrix location and density, since $T_{e,\text{sep}} \propto (1 - f_{\text{conv}})^{2/7}$. The leading coefficient also needs to be adjusted to align the *rev-2PM-detailed* $n_{e,\text{sep}}$ trend with the measurements, but otherwise the differences between the two sets of results are modest. It therefore seems rather fortuitous, as in the EDGE2D results, that the additional terms in the *rev-2PM-detailed* treatment compensate each other in a manner which largely balances their combined contributions in equations (3) and (4). These observations obtained utilizing the *model-based approximations* of the additional terms should not diminish the need to improve T_i measurements in the SOL, to further develop the $\lambda_q(\alpha_t)$ scaling with multi-machine datasets, and to develop a more complete picture of the dependence of the convective parallel heat flux contribution on divertor geometry, machine size and SOL plasma conditions.

6. More detailed EDGE2D assessment of the divertor configuration impact

So far we have not observed any clear evidence of a divertor configuration dependence in the H-mode correlations shown in [1] within measurement uncertainties and also in view of the less reliable $\langle T_{e,\text{ot}} \rangle$ estimates in the VV and CC configurations compared to the diagnostically optimized VH(C) configuration. Neither is there a clear divertor configuration dependent trend evident in the rev-2PM $n_{e,\text{sep}}$ comparisons for the H-mode and L-mode experiment data and EDGE2D results, except for the hypothetical CC(T6)-open configuration, for which a steeper $n_{e,\text{sep},2\text{PM}}$ slope is observed using the same leading coefficient. As noted in section 5.2, an increase in the $(1 - f_{\text{cooling}})/(1 - f_{\text{mom-loss}})$ ratio and τ_u reconciles this discrepancy. More generally, a wide open divertor geometry with large neutral leakage and correspondingly higher $n_{e,\text{sep}}$ at the OMP will, by definition (equation (1)), lead to a downward vertical shift of the $(1 - f_{\text{mom-loss}})$ trend at $\langle T_{e,\text{ot}} \rangle$ above the pressure-momentum loss onset. Hence, although the 2PM is clearly valuable for formatting code results and identifying the physical processes governing $n_{e,\text{sep}}$, it is of limited use for capturing the influence of large changes in divertor closure on $n_{e,\text{sep}}$ without *a priori* knowledge of the configuration specific $(1 - f_{\text{mom-loss}})$ volumetric losses, and thus $n_{e,\text{sep}}$ itself.

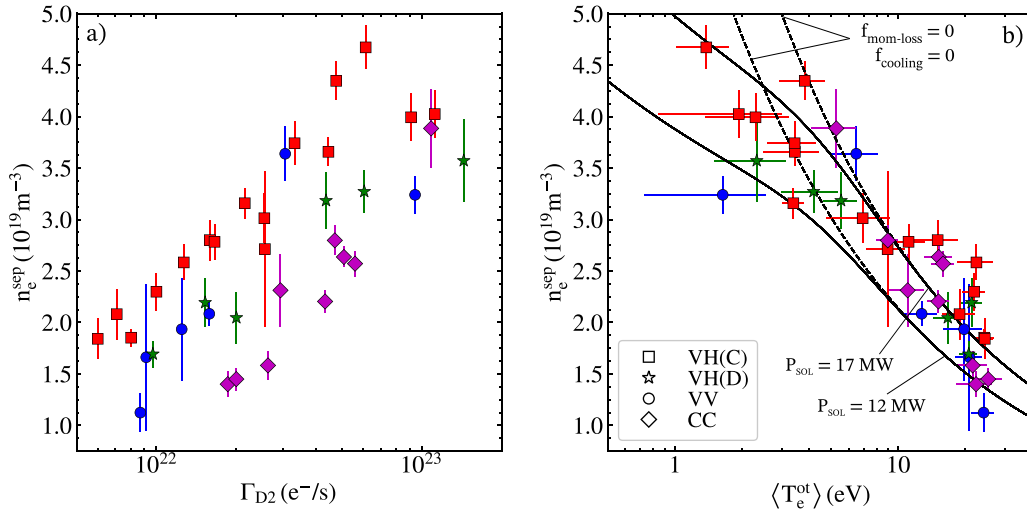


Figure 11. $n_{e,sep}$ vs D_2 fueling rate (a) and $\langle T_{e,ot} \rangle$ (b) for a subset of the H-mode dataset corresponding to 2 MA, 2.3 T discharges with P_{SOL} in the range 12–17 MW. The trend lines represent the 2PM $n_{e,sep}$ estimates at $P_{SOL} = 12$ and $P_{SOL} = 17$ MW including (full lines) and excluding (dashed lines) the $(1 - f_{mom-loss})$ and $(1 - f_{cooling})$ factors.

A common approach to examining the influence of divertor closure and magnetic configuration on $n_{e,sep}$ is to compare the onset of particle detachment (i.e. the rollover point of the total outer target ion current, $I_{div,ot}$) as a function of $n_{e,sep}$ (or $n_{e,ped}$), since $n_{e,sep}$ is typically considered to be the upstream driving parameter (e.g. [7, 16, 43, 44]). Given our present focus on correlations with the target electron temperature, we instead take the ‘bottom-up’ approach by examining the upstream conditions for a given value of $\langle T_{e,ot} \rangle$, since $n_{e,sep}$ (equation (3)) and $(1 - f_{mom-loss})$ and $(1 - f_{cooling})$ are strong functions of $T_{e,t}$. To isolate the divertor configuration impact as much as possible in the H-mode dataset, figure 11 shows a subset of the H-mode database $n_{e,sep}$ results for 2 MA, 2.3 T scenarios as a function of Γ_{D2} and $\langle T_{e,ot} \rangle$, with P_{sol} in the range 12–17 MW. Representative lines of best fit to the 2PM (equation (3)) are also shown in figure 11(b) for $P_{sol} = 12$ MW and $P_{sol} = 17$ MW to illustrate the influence of the $(1 - f_{cooling})/(1 - f_{mom-loss})$ ratio on suppressing the rising $n_{e,sep}$ trend at $\langle T_{e,ot} \rangle < 10$ eV. The $n_{e,sep} \propto P_{sol}^{5/7}$ dependence could not be clearly resolved within the scatter and uncertainties in this dataset due to the moderate range in P_{sol} . The configuration dependence of the 2 MA, 2.3 T $n_{e,sep}$ trends with Γ_{D2} are more clearly resolved in figure 11(a) compared to the results shown in [1] where the entire H-mode dataset was shown over a larger I_p range. In unifying these separate trends by replacing Γ_{D2} with $\langle T_{e,ot} \rangle$, there is some indication of higher $n_{e,sep}$ values for the VH(C) configuration at high $\langle T_{e,ot} \rangle$, which would be consistent with the more open geometry, but the limited data points and the greater likelihood of systematic errors in spectroscopic $\langle T_{e,ot} \rangle$ measurements at high values of electron temperature (>20 eV) in the different configurations preclude a more meaningful assessment. We therefore turn to the edge plasma simulations to further elucidate the divertor configuration impact on ionization patterns, neutral leakage and the role of main-chamber and divertor recycling on $n_{e,sep}$, given the general correspondence between the EDGE2D and experiment $n_{e,sep,2PM}$ results established in section 5.

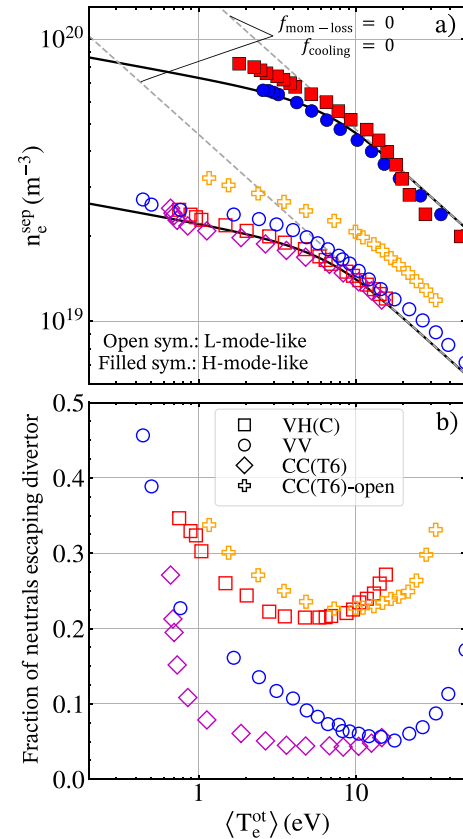


Figure 12. EDGE2D $n_{e,sep}$ vs $\langle T_{e,ot} \rangle$ trends for the L-mode-like (open symbols) and H-mode-like (filled symbols) and percentage of neutrals escaping the divertor vs $\langle T_{e,ot} \rangle$ for the L-mode-like dataset only (b).

Figure 12 shows $n_{e,sep}$ as a function of $\langle T_{e,ot} \rangle$ for the subset of the code results which includes: (a) the L-mode-like density scans in VH(C), VV, CC(T6) and CC(T6)-open with $P_{sol} = 3.5$ MW, fixed radial transport coefficients and

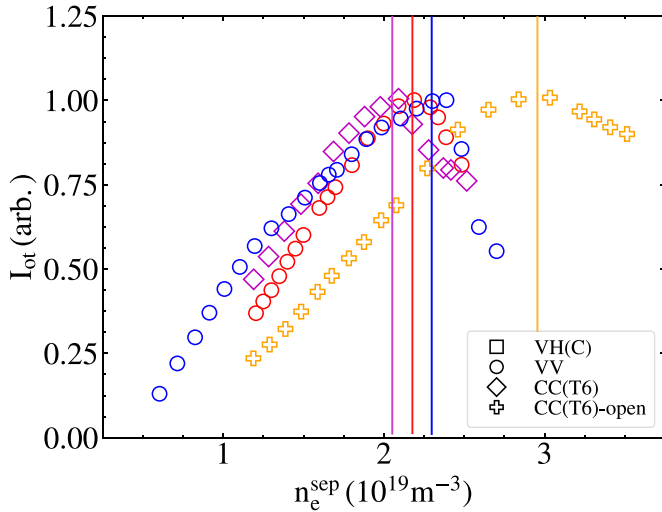


Figure 13. Peak normalized integrated outer target ion current vs $n_{e,sep}$ for the L-mode-like EDGE2D dataset. The vertical lines represent the approximate position of the ion current rollover.

otherwise identical inputs; and (b) the H-mode-like density scans in VH(C) and VV with $P_{sol} = 14$ MW, fixed radial transport coefficients constrained by experimental OMP n_e and T_e profiles in low-recycling conditions. The corresponding $n_{e,sep,2PM}$ lines of best fit for each power level are also shown with and without the volumetric momentum and cooling loss terms to highlight their importance in recovering the observed trends. While the differences in the radial transport coefficients and input powers between the L-mode-like and H-mode-like density scans give rise to a modest separation in the H-mode-like $n_{e,sep}$ vs $\langle T_{e,ot} \rangle$ trends between the VV and VH(C) configurations, the most significant difference is between the CC(T6)-open configuration and the other geometries in the L-mode like density scans. The CC(T6)-open configuration leads to a 50% increase in $n_{e,sep}$ for the entire $\langle T_{e,ot} \rangle$ range. This result is consistent with the differences in $n_{e,sep,2PM}$ shown in figure 8(b), and indicates that large changes in the divertor closure are required to break the unified $n_{e,sep}$ vs $\langle T_{e,ot} \rangle$ trends, or, conversely, that the VH(C), VV, CC(T6) configurations, despite their respective differences in closure and target inclination, lead to similar $n_{e,sep}$ values when mapped to $\langle T_{e,ot} \rangle$.

Recasting the EDGE2D $n_{e,sep}$ results into the more familiar $I_{div,ot}$ vs $n_{e,sep}$ trends, as shown in figure 13, further illustrates that only the CC(T6)-open divertor configuration leads to a marked increase in $n_{e,sep}$ at the $I_{div,ot}$ rollover point. It is important to note that, while both $\langle T_{e,ot} \rangle$ and $I_{div,ot}$ are useful experimentally derived parameters, the above trends do not capture the influence of target inclination and divertor closure on the details of the spatially resolved target parameters. A critical metric from the perspective of target survivability constraints is the peak heat flux deposited on the target, $q_{dep,t}^{peak}$. In this regard, the vertical target geometry has the beneficial feature of concentrating ionization sources close to the separatrix in the region of largest heat flux [36, 43, 45]. This effect has been observed in JET-ILW L-mode experiments in VV and VH(C) configurations [46] in which the VH(C) outer

target $T_{e,t}$ profile derived from LPs was found to be much more peaked compared to the VV $T_{e,t}$ profile, although this feature was not reproduced in an H-mode N_2 seeding study aimed at comparing the radiative divertor performance in VV and VH(C) configurations [47]. The influence of neutral pathways on the ionization distribution differences in the VV and VH(C) configurations was examined in more detail in [41] where the observed target T_e profile differences were attributed to the dominant role of reflected recycled neutrals from the HFS on the ionization distribution at the outer divertor separatrix in the VV configuration. Further efforts are needed to validate the target n_e , T_e , j_{sat} and $q_{dep,t}$ profiles predicted by 2D boundary plasma codes, including in the CC(T6) configurations, but such studies are challenging on JET-ILW due to diagnostic limitations and measurement uncertainties, and thus necessitate use of observables such as $\langle T_{e,ot} \rangle$ to constrain and evaluate the rev-2PM $n_{e,sep}$ description.

6.1. Neutral leakage from the divertor

To examine the role of neutral leakage from the divertor to the main-chamber on the OMP $n_{e,sep}$ we adopt the divertor leakage parameter (DLP) introduced in [7]. The DLP is defined as the ratio of the number of neutral particles escaping the divertor to the number of neutral particles born in the divertor, and is shown in figure 12(b) as a function of $\langle T_{e,ot} \rangle$ for the L-mode-like EDGE2D dataset. For each configuration, the DLP trends are characterized by an initial decrease in the escaping neutrals with decreasing $\langle T_{e,ot} \rangle$, followed by a reversal and eventual increase at low $\langle T_{e,ot} \rangle$. The VV and CC(T6) configurations exhibit similarly low levels (5%–20% in the range $1 \leq \langle T_{e,ot} \rangle \leq 10$ eV) of neutral leakage compared to the VH(C) and CC(T6)-open configurations, which show a factor of 2–4 increase in the DLP. Despite similar DLP trends and values for the VH(C) and CC(T6)-open cases, the 50% difference in their respective $n_{e,sep}$ values suggests that the DLP by itself cannot explain the $n_{e,sep}$ vs $\langle T_{e,ot} \rangle$ trends in figure 12(a).

The low field side (LFS) ionization distributions in the horizontal target configurations (VH(C), CC(T6) and CC(T6)-open), as shown in figure 14 for equal values of $\langle T_{e,ot} \rangle = 10$ eV, are characterized by an ionization region which, for the moderately open VH(C) and wide open CC(T6)-open configurations, extends into the outer SOL and above the X-point. In the CC(T6)-open configuration, the LFS ionization region extends to the OMP, similar to the DIII-D open configuration described in [7], while the presence of the outboard divertor baffle structure in the CC(T6) geometry, and to a lesser extent in the VH(C) geometry, obstructs recycled neutrals from spreading further upward into the main-chamber SOL. Hence, although the DLP trends and values are similar for the VH(C) and CC(T6)-open configurations, the larger extended ionization region in the CC(T6)-open case gives rise to a significantly higher $n_{e,sep}$ at the OMP. On the other hand, the ionization distribution in the VV geometry is significantly more concentrated near the inner and outer divertor legs along the separatrix, with comparatively little ionization extending above the X-point.

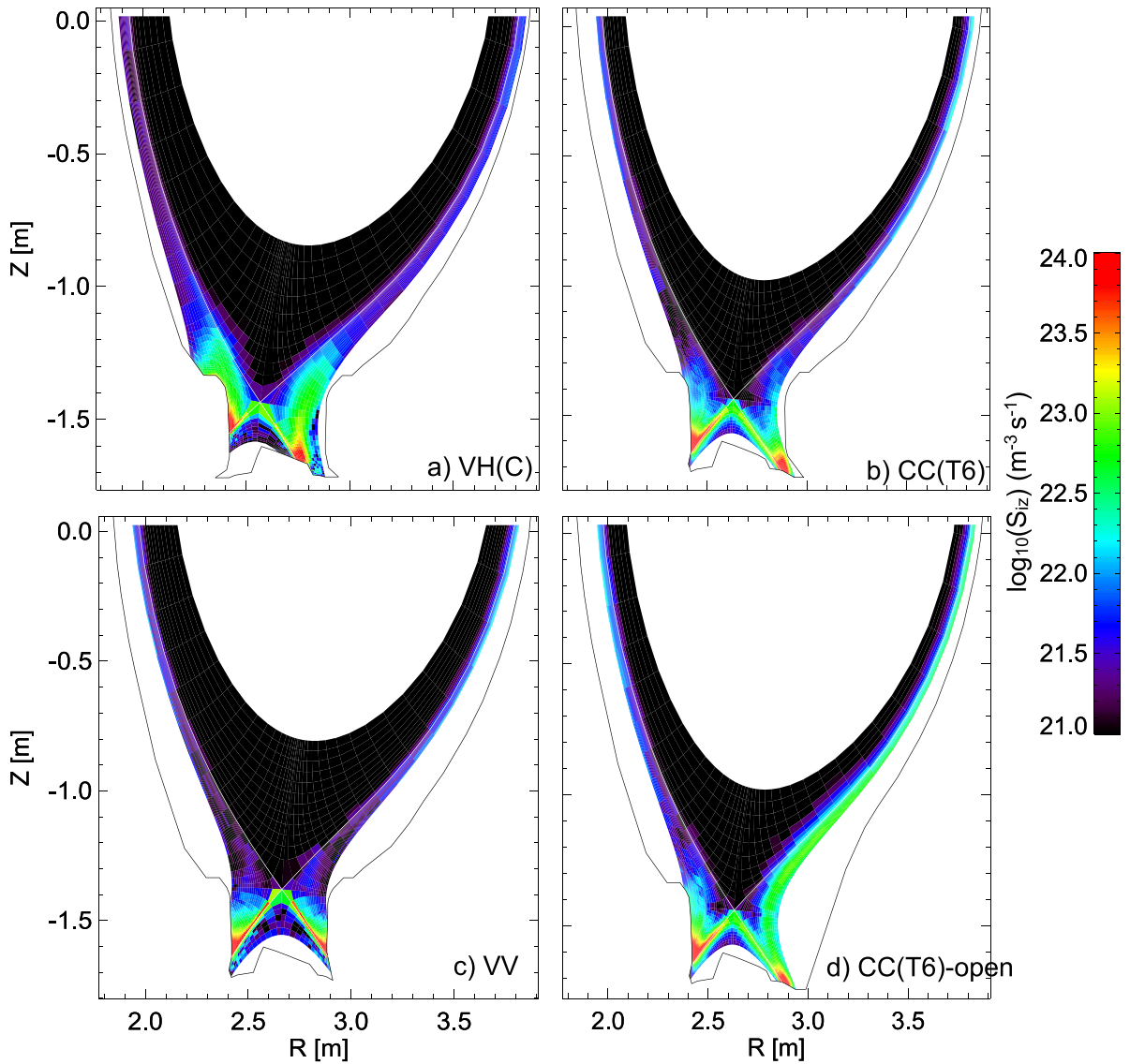


Figure 14. EDGE2D poloidal distribution of total ionization rate with $\langle T_{e,ot} \rangle = 10$ eV in the four divertor configuration cases.

6.2. Influence of MCR

A significant contribution to the neutral flux at the OMP region in the EDGE2D and SOLPS simulations is attributed to MCR of fuel species on the Be wall, for which a recycling coefficient of 1 is used in the model for ions and atomic neutrals. The MCR magnitude, however, is poorly constrained in the simulations as the scaling of the radial transport in the far-SOL is highly uncertain (e.g. see [48]). Additionally, the toroidally discrete JET-ILW HFS and LFS limiter geometry and their influence on the poloidally averaged MCR characteristics is also neglected in the 2D edge codes. While the MCR sensitivity with respect to changes in the outer SOL radial transport coefficients were not evaluated in the present study and clearly require extensive investigation, we proceed in this section to attempt to isolate the impact of the divertor configuration on $n_{e,sep}$. Taking a rather straightforward approach, we repeated the L-mode-like EDGE2D density scans with recycling of the fuel species ions on the main chamber Be wall turned off—i.e.

modifying the recycling coefficient from 1 to 0 on the Be main chamber wall. Recycling parameters on the divertor W surfaces and the pumping surfaces in the divertor corners were not modified. Such a setup represents an extreme case of recycling suppression on the vessel walls achieved in experiments using, for example, lithium coatings, which have been shown to reduce the recycling coefficient by $\sim 20\%$ [49]. Such active recycling control strategies are not used in JET-ILW, and hence turning off MCR in EDGE2D simulations is only intended to aid understanding.

The OMP $n_{e,sep}$ vs $\langle T_{e,ot} \rangle$ trends for the four divertor configurations with and without MCR are shown in figure 15. Excluding MCR leads to: (a) up to a factor of two overall reduction in $n_{e,sep}$ relative to results with MC recycling activated; and (b) a clear dependence on the divertor configuration, with $n_{e,sep}$ in the open VH(C) and CC(T6)-open configurations about 40% higher than in the more closed CC(T6) geometry, with the VV $n_{e,sep}$ trend spanning values in between the open

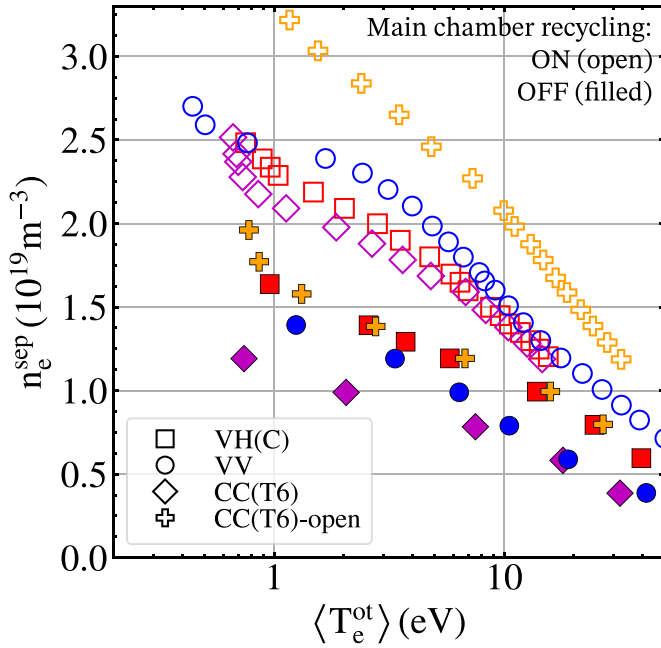


Figure 15. EDGE2D $n_{e,sep}$ vs $\langle T_{e,ot} \rangle$ trends for the L-mode-like simulations with main chamber recycling turned ON (open symbols) and OFF (filled symbols).

and closed horizontal configurations. These simulation results suggest that the MCR could have a moderating effect on the differences in the $n_{e,sep}$ vs $\langle T_{e,ot} \rangle$ trends imposed by the variation in divertor recycling patterns and ionization distributions. For instance, increasing closure has a clear influence on reducing the divertor recycling contribution to $n_{e,sep}$ in the VH(C) vs CC(T6) trends with MCR turned off, yet this benefit appears to be diminished in simulations with MCR turned on, at least when mapping $n_{e,sep}$ to $\langle T_{e,ot} \rangle$. Also, despite virtually identical trends for the VH(C) and CC(T6)-open results with MCR turned off, the larger extent of the ionization region in the LFS SOL (figure 14) clearly enhances the MCR at the OMP, resulting in an overall increase in $n_{e,sep}$ by 40%–50%. The contrast between the simulations with and without MCR is also illustrated in the poloidal distribution of the radial flux of neutrals through the separatrix shown in figure 16. In the absence of MCR, the separatrix and confined plasma regions are fueled entirely near the X-point region, with the neutral fluxes being more pronounced in the outer horizontal target VH(C) and CC(T6)-open configurations. Moreover, the absence of large neutral fluxes at the OMP due to MCR leads to $n_{e,sep}$ vs $\langle T_{e,ot} \rangle$ trends that are consistent with the DLP neutral leakage trends shown in figure 12(b), in which enhanced closure and vertical target orientation have a pronounced effect in reducing $n_{e,sep}$ for the same $\langle T_{e,ot} \rangle$ values. Since these configuration dependent $n_{e,sep}$ trends are not observed in experiment (figure 11(b)), we infer that a significant contribution to $n_{e,sep}$ arising from MCR is more consistent with the measurements.

The above analysis does not provide information on the composition of the MCR particle fluxes, which can be attributed to a combination of thermal release of neutrals from the recycled radial plasma flux, reflected charge exchange

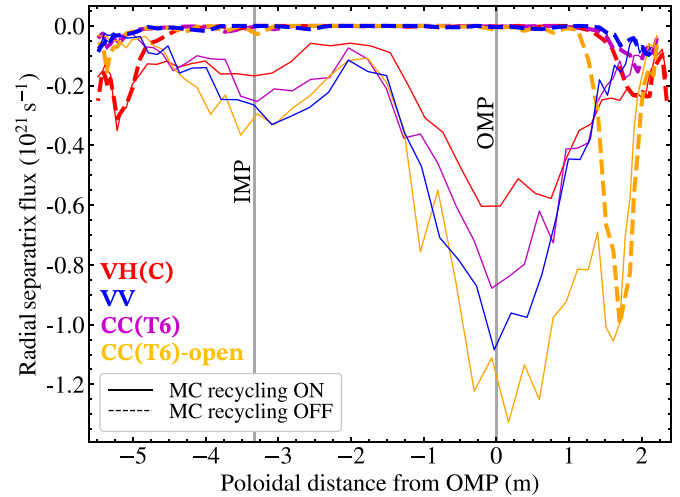


Figure 16. Poloidal profiles of the neutral flux crossing the separatrix for EDGE2D L-mode-like cases at $\langle T_{e,ot} \rangle = 10$ with and without main chamber recycling.

neutrals, reflected ballistic neutrals which originate in the LFS or HFS divertor, as well as volume recombination of ions. The extent to which the recycled neutrals from divertor targets contribute to the OMP ionization profile depends on the geometric screening/baffling, as well as the physical size of the divertor and the ionization mean-free path for a given plasma solution. In a recent SOLPS-ITER numerical study of an AUG L-mode density ramp discharge, Zito *et al* [26] showed that the dominant contribution to the OMP ionization profile is attributed to the neutral flux originating from recycling at the outer and inner divertor, whereas the MCR component was shown to be small. As acknowledged in the study, these results contrast with an earlier study on the far SOL density shoulder formation by Lunt *et al* [50], in which a different modelling package was used, EMC3-EIRENE, featuring a computational grid which extends up to the physical wall. The uncertainty in the composition of the MCR flux could therefore be linked to the grid limitations in code packages such as SOLPS and EDGE2D, in which the computational grids do not extend fully to the wall surfaces.

As already mentioned in the companion paper [1], the divertor size scaling and neutral compression also likely have a strong influence on the divertor recycled neutrals coupling to the OMP plasma fueling. This has been illustrated in a numerical study [12] comparing full scale and scaled down (1/3 size) ITER SOLPS-ITER simulations. These simulations indicate that, whereas the divertor neutral pressure is effectively decoupled from $n_{e,sep}$ in the full size ITER scenario due to the large divertor size, in the scaled down ITER cases, $n_{e,sep}$ and the ionization fraction in the main chamber increase monotonically with rising divertor neutral pressure. However, the influence of the radial plasma flux from MCR on $n_{e,sep}$ is not clearly identified in the study, since a decomposition of the type carried out in [26] was not attempted.

Following the methodology in [26], we carried out a similar decomposition of the OMP ionization profile, shown

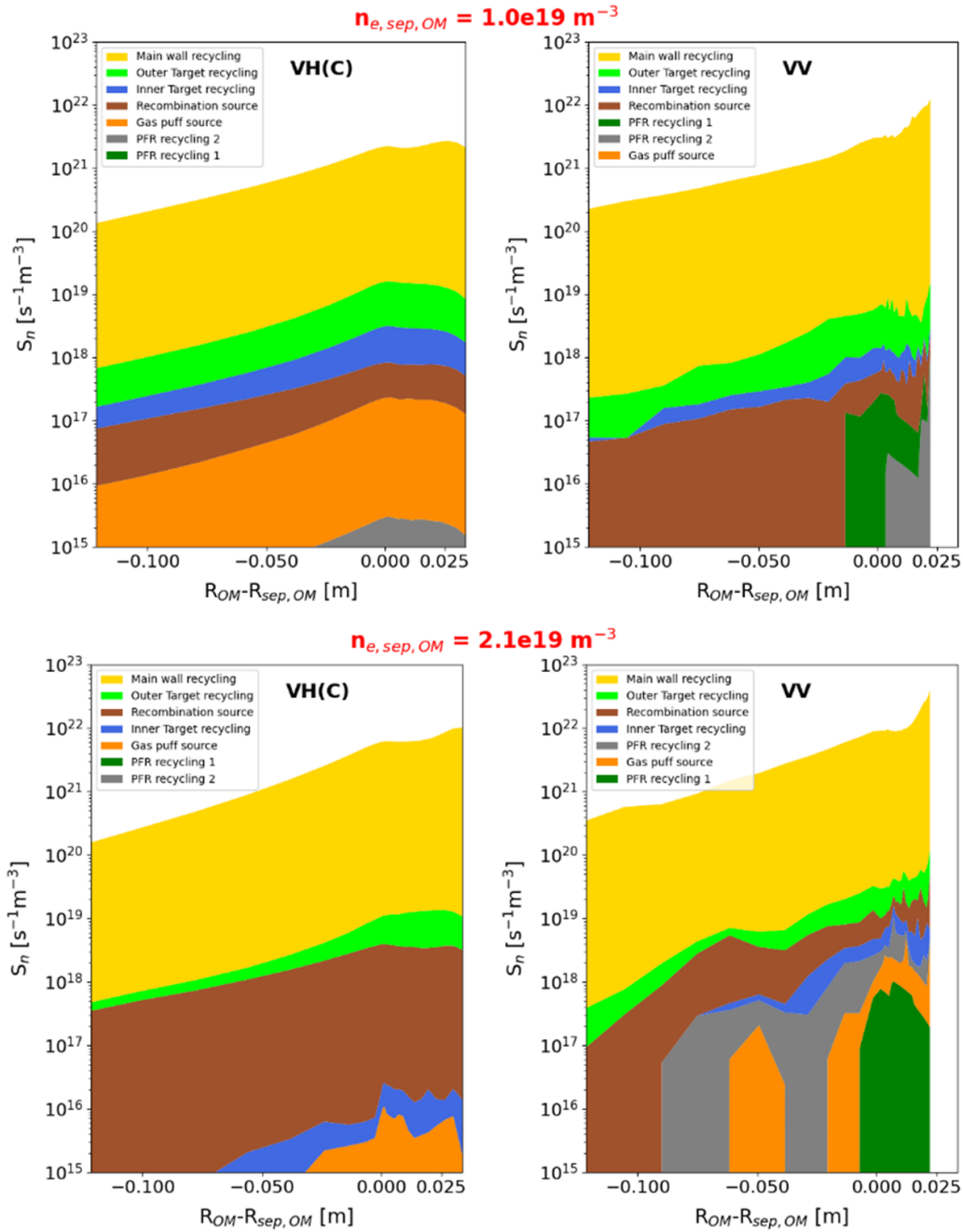


Figure 17. SOLPS-ITER L-mode-like decomposition of the outer midplane ionization radial profile based on the origin of ionized neutrals for low and high $n_{e,sep,OM}$ cases in the VV and VH(C) divertor configurations.

in figure 17, using the SOLPS-ITER L-mode-like cases in JET-ILW VH(C) and VV configurations. In contrast to the findings in the AUG SOLPS-ITER simulations, the JET-ILW results indicate that the dominant ionization contribution is from MCR for the entire range of the density scan, whereas the contributions from the inner and outer divertor recycling are found to be two orders of magnitude smaller. Assuming that the dominance of the MCR radial plasma flux contribution to the OMP ionization profile is not invalidated by transport and grid extension modifications, the small contribution to the OMP ionization profile from ballistic neutrals recycled in the divertor would be consistent with the larger size of JET,

and increased neutral compression, in accordance with the full scale and AUG-sized ITER simulations in [12].

Although SOLPS-ITER simulations of the CC(T6)-open configuration were not carried out, it is also reasonable to assume that the considerably more open geometry, and the 50% increase in $n_{e,sep}$ relative to the VH(C) configuration, gives rise to a larger contribution from outer divertor recycled neutrals, which have a more direct path through the cold outer SOL plasma to the OMP region compared to the other configurations.

Measurements of the MCR magnitude and OMP ionization profiles from, for example, spatially resolved main chamber

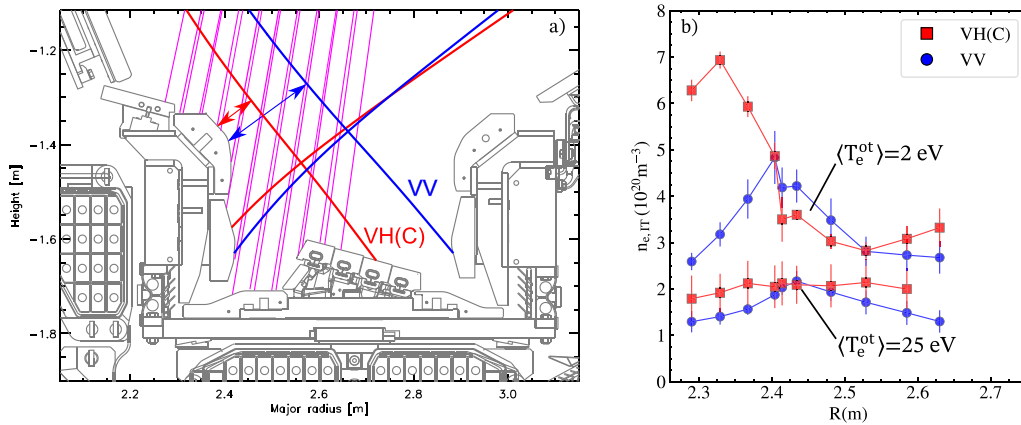


Figure 18. (a) Inner divertor spectroscopic lines of sight and magnetic configurations of the VH(C) and VV geometries showing the relative clearance from the inner divertor baffle to the separatrix; (b) electron density profiles inferred from Stark broadening of the D_δ Balmer line for the 2 MA, 2.3 T, $P_{\text{NBI}} = 15\text{--}16$ MW and $P_{\text{IRCH}} = 2\text{--}3$ MW subset of the H-mode dataset corresponding to $\langle T_{e,ot} \rangle = 25$ and 2 eV.

D_α emission from tangentially viewing filtered cameras, could provide important modelling constraints. Inversion and interpretation challenges in the analysis of such measurements due to wall reflections and toroidally discrete limiters on JET are being currently addressed but are outside the scope of the present study. The influence of ballooning transport (i.e. poloidally varying radial transport coefficients) on the poloidal variation in the particle flux has also been neglected in the EDGE2D and SOLPS-ITER modelling. Further studies incorporating the above considerations are needed to more fully evaluate the dependence of $n_{e,sep}$ trends on machine size and divertor geometry.

6.3. Influence of the inner divertor conditions

In the foregoing analysis we have so far ignored the conditions at the inner target and how these may be correlated with $\langle T_{e,ot} \rangle$ and $n_{e,sep}$. From a practical standpoint, the inner target is relatively poorly diagnosed compared to the outer target, particularly due to a lack of spectroscopic $\langle T_{e,it} \rangle$ measurements. From the modelling perspective, the inner target conditions are also more sensitive to drift effects [18, 51, 52] when $B \times \nabla B$ is directed towards the divertor, as is the case for JET-ILW discharges.

The formation of a high-field side high density region (HFSHD) observed on AUG [53–55] has been linked to changes in the fueling of the confined plasma and the neutral particle source distribution in an interpretive SOLPS 5.0 modelling study by Reimold *et al* [56]. The presence of the HFSHD region was found to change the poloidal asymmetry of the IMP and OMP plasma profiles, and leads to changes in the balance of the inward and outward directed drift-driven particle flows across the separatrix, thus modifying the ionization distribution and flow patterns in the SOL. The changes in the confined plasma fueling due to the presence of the HFSHD region have potential implications on plasma performance as well [57, 58], with a strong correlation observed between the reduction of the HFSHD front via N_2 seeding and improvement in plasma confinement, thought to be linked to radial shifts in the pedestal

density profile. The HFSHD formation has also been observed on JET-ILW in H-mode discharges with sufficiently high heating power using inner divertor spectroscopic D_δ Stark broadening electron density measurements in the VV configuration [55]. However, a detailed interpretive modelling study has not been attempted on JET-ILW to elucidate the influence of the HFSHD region on the ionization distribution, separatrix and confined plasma fueling, made even more challenging given the lack of IMP plasma profile information and neutral pressure gauges in the JET vessel in contrast to the relatively better diagnosed inner SOL region in AUG.

By comparing the VV and VH(C) configurations, we observe that changes in the magnitude of the HFSHD region have little effect on the upstream parameter correlations when mapped to $\langle T_{e,ot} \rangle$. Although the ISP in these configurations is in a similar position on the inner vertical target (tile 3), the clearance between the inner divertor shoulder tile and the separatrix in the VH(C) configuration is less than half of that in the VV configuration (8 cm vs 20 cm, see figure 18(a)). This reduced clearance has been linked to surface overheating and outgassing of fuel species neutrals trapped in Be co-deposits which tend to accumulate there [59, 60]. The reduced clearance to the separatrix in the VH(C) configuration leads to increased heat flux reaching tile 1 during the ELM cycle, increasing the surface temperature and thus providing a transient source of neutrals that desorb from the Be co-deposits. Significant differences in the inner divertor density profiles, $n_{e,it}$, between the two configurations are shown in figure 18(b) at two values of $\langle T_{e,ot} \rangle \approx 25$ and 2 eV. Whereas the $n_{e,it}$ radial profiles are of similar magnitude and spatial distribution at $R_{\text{maj}} > 2.4$ m outboard of the ISP, there is a significant increase in $n_{e,it}$ at $R_{\text{maj}} < 2.4$ m in the VH(C) configuration, which is physically located above the inner divertor shoulder (tile 1). Despite this more pronounced HFSHD region in the VH(C) configuration, however, no clear influence of the HFSHD interaction with the confined plasma is observed in the OMP upstream parameter correlations with $\langle T_{e,ot} \rangle$ in [1] (e.g. $p_{e,ped}$ vs $\langle T_{e,ot} \rangle$ and $n_{e,sep}$ vs $\langle T_{e,ot} \rangle$ for the entire low triangularity H-mode dataset).

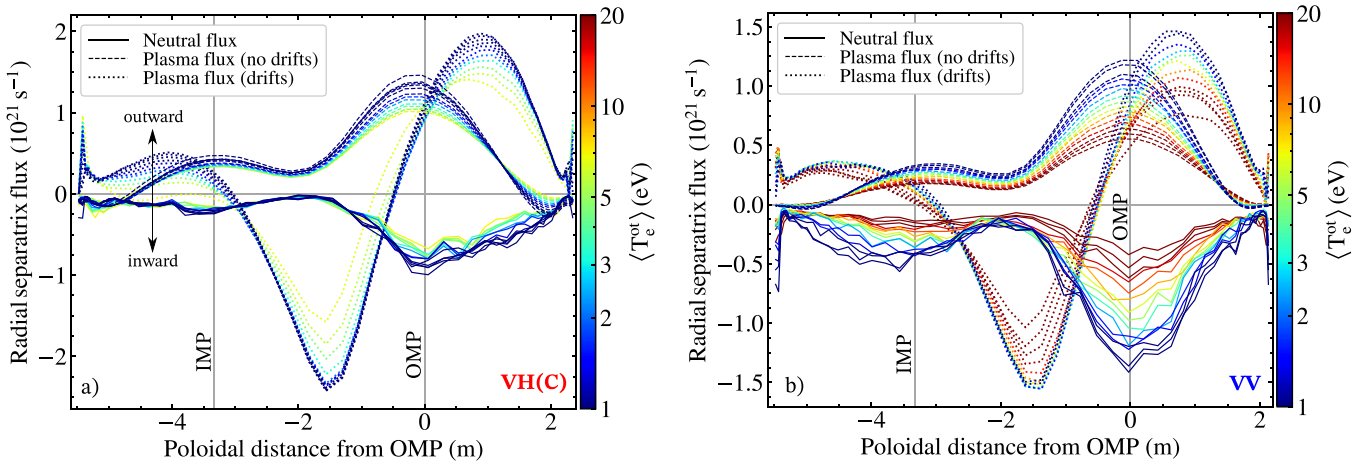


Figure 19. Poloidal distribution of the particle fluxes across the separatrix for the EDGE2D L-mode-like VH(C) and VV simulations. In the cases with drifts, the radial plasma flux is composed of both a diffusive component driven by inverted density gradients and the drift-driven convective flow component. The neutral flux is representative of cases with and without drifts.

One caveat to this interpretation is the possible HFS-LFS divertor plasma coupling in examining the influence of the HFSHD on the upstream parameter trends mapped to $\langle T_{e,ot} \rangle$. In looking at the different pathways of recycled neutrals in the JET-ILW VH(C) configuration, Moulton *et al* [41] found that the outer divertor ionization distribution was largely independent of the influence of neutrals originating in the inner divertor, whereas the contribution of the inner divertor neutrals to the ionization source near the outer divertor leg in the VV configuration was shown to be significant, but less so away from the separatrix. Hence, this numerical study suggests that while in the VH(C) configuration $\langle T_{e,ot} \rangle$ is likely decoupled from the details of recycling patterns in the inner divertor, the same cannot be said for the VV configuration, in which $\langle T_{e,ot} \rangle$ could be influenced to some degree by the neutral source in the inner divertor.

Modelling the influence of the tile 1 outgassing mechanism on the plasma solution and poloidal fueling profile poses significant challenges due to the transient ELM-induced desorption of the fuel particle source contained in the Be co-deposits. Capturing these mechanisms necessitates more sophisticated time-dependent simulations and modified recycling and reservoir models capturing Be erosion, migration and co-deposition, and surface temperature evolution, features which are currently under development for the SOLPS-ITER package, for example [59]. Although the dynamics of the inner divertor outgassing are not captured in the EDGE2D L-mode-like density scans, the simulations are still useful for examining the influence of drifts on the HFS JET-ILW plasma and poloidal fueling profile, shown to be a critical ingredient in capturing the HFSHD formation and impact on the SOL plasma in AUG [56]. In higher heating power discharges the cross-field $E_\theta \times \mathbf{B}$ drift drive will be stronger since $E_\theta \propto dT/ds$ and $T_{e,sep} \geq 100$ eV compared to the low power EDGE2D cases with $P_{in} = 2.2\text{--}3.8$ MW and $50 \leq T_{e,sep} \leq 70$ eV. Nevertheless, the L-mode-like low power EDGE2D cases with drifts activated still serve as an instructive example.

Similar to figure 3 in [56], figure 19 shows the poloidal distribution of the radial fluxes crossing the separatrix, including the inward flux of neutrals fueling the confined plasma, as well as the inward/outward radial plasma flux, for the VV and VH(C) density (or $\langle T_{e,ot} \rangle$) scans with and without drifts activated. In the cases with drifts activated, the radial plasma flux is composed of both the diffusive component driven by density gradients, and a convective component due to drifts. The changes in the balance of the inward and outward plasma flux due to drift activation discussed in [56] are reproduced in these EDGE2D simulations, yielding a strong inward plasma flux fueling the plasma near the top of the vessel, and a more outward dominated plasma flux near the X-point on both the LFS and HFS. Apart from the magnitude of the fluxes, which increase with increasing density (or decreasing $\langle T_{e,ot} \rangle$), these poloidal fueling patterns are present in both VV and VH(C) configurations, and over the entire $\langle T_{e,ot} \rangle$ range, albeit using fixed radial transport coefficients. The poloidal distribution and magnitude of the inward neutral fluxes through the separatrix are not found to be sensitive to the activation of drifts. As such, while drifts clearly play an important role in increasing the radial plasma flux contribution to the total confined plasma fueling, there is no indication that the presence of a HFSHD region is necessary for these changes in the inward and outward drift-driven radial plasma fluxes to manifest. However, a detailed interpretive modelling effort simultaneously reconciling both LFS and HFS SOL and divertor plasma conditions, such as the one presented in [56], is not attempted here, and is hindered by the lack of neutral pressure gauges. Despite these shortcomings, combining (a) the absence of a clear influence of the VH(C) tile 1 outgassing on the H-mode OMP $n_{e,sep}$ vs $\langle T_{e,ot} \rangle$ trends from experiment, with (b) observation of a consistent change in the poloidal plasma fueling profile imposed by drift-driven plasma fluxes present at both low and high densities in the VV and VH(C) EDGE2D L-mode-like simulations, there is so far no clear indication that the HFSHD region is playing a significant role in modifying the OMP edge density in JET-ILW discharges. Further studies

looking for changes to the radial shifts in the density profiles in the VH(C) and VV configurations are needed to compare to the observations on AUG in which a strong correlation between the formation of the HFSHD front and radial shifts in the pedestal density profile were linked with a reduction in pedestal pressure [57].

7. Summary and conclusions

In this report we have characterized the primary drivers for the OMP $n_{e,sep}$ and the strong dependence on the outer divertor target electron temperature in unseeded JET-ILW plasmas, thus linking the transport and recycling mechanisms on open field lines to the observed core and pedestal parameter and global confinement correlations with the averaged outer target electron temperature, $\langle T_{e,ot} \rangle$, described in the companion paper [1].

Recognizing the importance of $n_{e,sep}$ as an interface parameter between the SOL-divertor and the confined plasma regions, we have employed the rev-2PM to estimate $n_{e,sep}$ with an explicit dependence on $\langle T_{e,ot} \rangle^{-1/2}$ arising from parallel pressure balance, as well as on the ratio of the power and momentum volumetric loss factors, $(1 - f_{cooling})/(1 - f_{mom-loss})$, which also exhibits a primary dependence on the outer target electron temperature. Quantifying the influence of the $(1 - f_{cooling})$ and $(1 - f_{mom-loss})$ loss factors on $n_{e,sep}$ has been enabled by measurements of these quantities from L-mode density ramps in the outer horizontal, VH(C), and vertical target, VV, divertor configurations. The measured onset of cooling and momentum losses at $\langle T_{e,ot} \rangle = 3\text{--}10$ eV, as well as a moderately steeper falloff in the VV configuration, are generally consistent with EDGE2D L-mode-like density scan simulations. However, the interpretation and post-processing details of the simulation output have a moderate impact on the agreement with the measured $(1 - f_{cooling})$ and $(1 - f_{mom-loss})$ trends.

In applying the rev-2PM to recover the measured $n_{e,sep}$ trends, two approaches are considered. In the *rev-2PM-simplified* approach the widening of the power width in the near-SOL with increasing collisionality is ignored and instead the ITPA H-mode λ_q scaling is used. The convective contribution to the upstream parallel heat flux, f_{conv} , is also ignored, and the upstream $T_i/T_e = 2$ is assumed to be a constant while at the target T_i is assumed to be equal to T_e . These simplifications are necessary due to a limited set of measurements in the SOL and divertor. The *rev-2PM-simplified* $n_{e,sep}$ estimates for the extended H-mode dataset are recovered to within $\pm 25\%$, once a scaling factor of 0.2 is applied to account for the fact that $\langle T_{e,ot} \rangle$, an averaged quantity, is used to relate the downstream conditions to the OMP $n_{e,sep}$, whereas the 2PM is intended to be applied on a flux tube resolved basis. A similar factor of 0.3 is obtained by following the same *rev-2PM-simplified* interpretation in post-processing EDGE2D H-mode-like density scans in the VH(C) and VV configurations, lending confidence to the rev-2PM in capturing the dominant processes driving $n_{e,sep}$. The impact of f_{conv} and T_i/T_e on recovering $n_{e,sep}$ with the rev-2PM was estimated using the

EDGE2D density scans and mapped as approximate functions of $\langle T_{e,ot} \rangle$. These additional terms derived from the simulations were applied in the *rev-2PM-detailed* model in addition to the recently developed collisionality dependent $\lambda_q(\alpha_t)$ scaling from AUG [22]. While each term in isolation was found to be significant, their combined effect was found to have only a modest impact on recovering the measured $n_{e,sep}$ values. Further studies are needed to clarify how general this result is, as f_{conv} , for example, is found to be more pronounced in the VH(C) configuration compared to VV, in line with expectations of higher upstream ionization in more open divertor geometries. The $\lambda_q(\alpha_t)$ scaling derived from an AUG dataset has also not been tested on other machines at the time of writing.

In the H-mode dataset, we observed that the $(1 - f_{cooling})/(1 - f_{mom-loss})$ ratio in the rev-2PM has only a moderate impact on recovering the measured $n_{e,sep}$ due to operational constraints in reaching deep detachment via increasing D_2 fueling. In the L-mode dataset, however, this ratio as a function of $\langle T_{e,ot} \rangle$ is observed to be critical for reconciling the measured $n_{e,sep}$ for $\langle T_{e,ot} \rangle < \sim \text{few eV}$ since lower target temperatures and more pronounced detachment were accessed. Hence, in unseeded neutral-plasma interaction dominated detachment with $\langle T_{e,ot} \rangle$ of a few eV, the $(1 - f_{cooling})/(1 - f_{mom-loss})$ ratio constitutes the dominant $n_{e,sep}$ driving term. Conversely, at $\langle T_{e,ot} \rangle > 10$ eV, the $n_{e,sep} \propto \langle T_{e,ot} \rangle^{-1/2}$ term dominates, and consequently the pronounced reduction in $H_{98(y,2)}$ with rising $n_{e,sep}$ and decreasing $\langle T_{e,ot} \rangle$ from 30 to 10 eV shown in [1] is mainly attributed to parallel pressure balance as the target pressure and recycling particle flux rise with increasing D_2 fueling rates.

In the H-mode upstream parameter correlations with $\langle T_{e,ot} \rangle$ shown in [1], a clear divertor configuration dependence could not be distinguished. Similarly, the rev-2PM estimates in VV, VH(C) and the outer corner, CC(T6), configurations do not appear to be sensitive to the range of divertor geometries available on JET-ILW. We examined the divertor configuration effect in more detail using the EDGE2D L-mode-like density scans and observed that MCR is likely playing a significant role in moderating $n_{e,sep}$ to changes in divertor neutral leakage imposed by changes in the divertor configuration. The MCR magnitude, however, is poorly constrained in simulations due to large uncertainties in outer SOL radial transport and difficulties in main chamber edge plasma diagnostic interpretation. When MCR of fuel species on the Be wall is turned off in simulations, the $n_{e,sep}$ trends diverge in a manner consistent with divertor neutral leakage patterns, i.e. increased closure leads to reduced $n_{e,sep}$ for the same $\langle T_{e,ot} \rangle$, and a vertical target orientation is similarly beneficial. Conversely, when MCR is turned on in simulations, $n_{e,sep}$ increases by 40%–70%, and the configuration dependent trends are no longer discernible, which is more consistent with the $n_{e,sep}$ measurements in experiment. A decomposition of the midplane ionization profile in like-for-like SOLPS-ITER simulations revealed that the main chamber neutrals originate predominantly from recycled radial plasma flux on the main chamber wall, rather than from the divertor. An additional EDGE2D density scan was carried out using a hypothetical divertor geometry (CC(T6)-open) in which the

entire low field side baffle was removed to test the response of the $n_{e,sep}$ trend to a large geometry change. In the CC(T6)-open geometry the combination of large outboard divertor neutral leakage and MCR leads to a further 40% increase in upstream density relative to the other configurations, thus confirming that a large change to the JET-ILW divertor geometry is needed, beyond the range of available configurations, to break the observed $n_{e,sep}$ vs $\langle T_{e,ot} \rangle$ trends. We note that the spatially resolved details of divertor target parameters including the target heat fluxes, although not examined in this study due to measurement limitations, are expected to be impacted by the target orientation, as shown in numerical studies [17, 41].

The lack of divertor configuration dependence in the $p_{e,ped}$ vs $\langle T_{e,ot} \rangle$ trends shown in [1] and $n_{e,sep}$ vs $\langle T_{e,ot} \rangle$ trends also suggests that the formation of the HFSD region does not significantly influence the OMP pedestal pressure and separatrix density, despite the large differences in the clearance between the inner divertor and separatrix among the divertor configurations. This clearance is especially narrow in the VH(C) configuration, which leads to a previously observed enhanced ELM-induced particle source from fuel species outgassing from Be co-deposits on top of the inner divertor and higher inner divertor densities compared to the VV configuration. Further studies are needed to assess potential changes in radial shifts in the OMP density profiles in the VH(C) and VV configurations, following similar observations on AUG.

Although modelling the transient outgassing physics is outside the scope of this work, we further investigated the role of the inner divertor high density formation by comparing EDGE2D vertical and outer horizontal configuration L-mode-like density scans with drifts activated. The role of drifts has been previously shown in [56] to be crucial for recovering the higher inner divertor density conditions typically observed in experiments with the $\mathbf{B} \times \nabla B$ direction towards the divertor. However, the EDGE2D simulations show that while drift-driven plasma fluxes change the distribution of the poloidal plasma fueling profile considerably, these changes are present in both configurations, and also over the entire range of the density scan and are therefore independent from the evolution of the inner divertor density. The assumption of constant radial transport throughout the entire density scans, and the low power conditions amenable to numerical convergence in these drift-activated cases warrant more detailed analysis of these mechanisms.

In future work further application of the rev-2PM analysis to ITER edge plasma simulations as well as multi-machine experiment and simulation datasets could improve understanding of the $n_{e,sep}$ dependence on machine size, the extent of the MCR and divertor baffling influence on $n_{e,sep}$, and the variation of the $(1 - f_{cooling})/(1 - f_{mom-loss})$ ratio in optimizing highly radiative impurity seeded scenarios as a possible power exhaust solution. Contrasting the divertor neutral pressure based $n_{e,sep}$ model developed on AUG [8] with the target electron temperature based description presented herein would further advance the development of $n_{e,sep}$ scaling from the perspective of both the dominant engineering and physics parameters.

Acknowledgments

This work has been carried out within the framework of the EUROfusion Consortium, funded by the European Union via the Euratom Research and Training Programme (Grant Agreement No 101052200—EUROfusion). Views and opinions expressed are however those of the author(s) only and do not necessarily reflect those of the European Union or the European Commission. Neither the European Union nor the European Commission can be held responsible for them. This work was also supported by the US DOE under Contract No. DE-AC05-00OR22725 with UT-Battelle, LLC. This scientific paper has been published as part of the international project co-financed by the Polish Ministry of Science and Higher Education within the programme called ‘PMW’ for 2021.

ORCID iDs

B. Lomanowski  <https://orcid.org/0000-0003-2226-2004>
 G. Rubino  <https://orcid.org/0000-0002-4157-6327>
 A. Uccello  <https://orcid.org/0000-0003-3044-1715>
 M. Dunne  <https://orcid.org/0000-0002-5259-9970>
 N. Vianello  <https://orcid.org/0000-0003-4401-5346>
 S. Aleiferis  <https://orcid.org/0000-0001-7529-470X>
 J. Canik  <https://orcid.org/0000-0001-6934-6681>
 I. Carvalho  <https://orcid.org/0000-0002-2458-8377>
 L. Frassinetti  <https://orcid.org/0000-0002-9546-4494>
 L. Garzotti  <https://orcid.org/0000-0002-3796-9814>
 M. Groth  <https://orcid.org/0000-0001-7397-1586>
 A. Meigs  <https://orcid.org/0000-0002-8071-864X>
 C. Perez von Thun  <https://orcid.org/0000-0002-1166-2179>
 P.A. Schneider  <https://orcid.org/0000-0001-7257-3412>
 G. Sergienko  <https://orcid.org/0000-0002-1539-4909>
 J. Simpson  <https://orcid.org/0000-0002-0083-9637>
 D. Van Eester  <https://orcid.org/0000-0002-4284-3992>

References

- [1] Lomanowski B. et al 2022 *Nucl. Fusion* **62** 066030
- [2] Frassinetti L. et al 2017 *Nucl. Fusion* **57** 016012
- [3] Stangeby P.C. 2018 *Plasma Phys. Control. Fusion* **60** 044022
- [4] Stangeby P.C. et al 2021 The role of the target electron temperature as a key detachment parameter 63rd Annual Meeting of the APS Division of Plasma Physics (Pittsburgh, USA) (available at: <https://meetings.aps.org/Meeting/DPP21/Session/CT02.1>)
- [5] Moser A.L., Leonard A.W., McLean A.G., Wang H.Q. and Watkins J.G. 2019 *Nucl. Mater. Energy* **19** 67–71
- [6] Casali L., Covele B.M. and Guo H.Y. 2019 *Nucl. Mater. Energy* **19** 537–43
- [7] Casali L., Eldon D., Boedo J.A., Leonard T. and Covele B. 2020 *Nucl. Fusion* **60** 076011
- [8] Kallenbach A. et al 2018 *Plasma Phys. Control. Fusion* **60** 045006
- [9] Kallenbach A. et al 2019 *Nucl. Mater. Energy* **18** 166–74
- [10] Leonard A.W., McLean A.G., Makowski M.A. and Stangeby P.C. 2017 *Nucl. Fusion* **57** 086033
- [11] Pitts R.A. et al 2019 *Nucl. Mater. Energy* **20** 100696
- [12] Park J.S., Bonnin X. and Pitts R. 2019 Assessment of ITER W divertor performance during early operation phases 61st

- Annual Meeting of the APS Division of Plasma Physics (Fort Lauderdale, USA) (PO5)*
- [13] Park J.S., Bonnin X. and Pitts R. 2021 *Nucl. Fusion* **61** 016021
- [14] Pasqualotto R. *et al* 2004 *Rev. Sci. Instrum.* **75** 3891
- [15] Wiesen S. 2006 EDGE2D/EIRENE code interface report (available at: http://eirene.de/e2deir_report_30jun06.pdf)
- [16] Groth M. *et al* 2013 *Nucl. Fusion* **53** 093016
- [17] Groth M. *et al* 2015 *J. Nucl. Mater.* **463** 471–6
- [18] Lomanowski B. *et al* 2019 *Nucl. Mater. Energy* **20** 100676
- [19] Lomanowski B. *et al* 2020 *Plasma Phys. Control. Fusion* **62** 065006
- [20] Wiesen S. *et al* 2015 *J. Nucl. Mater.* **463** 480–4
- [21] LaBombard B. *et al* (Team TACM) 2005 *Nucl. Fusion* **45** 1658–75
- [22] Eich T. *et al* 2020 *Nucl. Fusion* **60** 056016
- [23] Carralero D. *et al* 2017 *Nucl. Mater. Energy* **12** 1189–93
- [24] Wynn A. *et al* 2018 *Nucl. Fusion* **58** 056001
- [25] Wiesen S. *et al* 2011 *J. Nucl. Mater.* **415** S535–9
- [26] Zito A. *et al* 2021 *Plasma Phys. Control. Fusion* **63** 075003
- [27] Pitcher C.S. and Stangeby P.C. 1997 *Plasma Phys. Control. Fusion* **39** 779–930
- [28] Stangeby P.C. 2000 *The Plasma Boundary of Magnetic Fusion Devices* (Bristol: Institute of Physics Publishing)
- [29] Stangeby P. 2020 *Plasma Phys. Control. Fusion* **62** 025013
- [30] Eich T. *et al* 2013 *Nucl. Fusion* **53** 093031
- [31] Stagni A. *et al* 2022 *Nucl. Fusion* **62** 096031
- [32] Horacek J. *et al* 2020 *Nucl. Fusion* **60** 066016
- [33] Tskhakaya D. *et al* 2008 *Contrib. Plasma Phys.* **48** 89–93
- [34] Brunner D. *et al* 2013 *Plasma Phys. Control. Fusion* **55** 095010
- [35] Kotov V. *et al* 2008 *Plasma Phys. Control. Fusion* **50** 105012
- [36] Lipschultz B., LaBombard B., Terry J.L., Boswell C. and Hutchinson I.H. 2007 *Fusion Sci. Technol.* **51** 369–89
- [37] Paradel Pérez I., Scarabosio A., Groth M., Wischmeier M. and Reimold F. 2017 *Nucl. Mater. Energy* **12** 181–6
- [38] Lomanowski B. *et al* 2022 Variation in the volumetric power and momentum losses in the JET-ILW scrape-off layer *Nucl. Mater. Energy* submitted
- [39] Huber A. *et al* 2007 *J. Nucl. Mater.* **363–365** 365–70
- [40] Greenwald M. 2002 *Plasma Phys. Control. Fusion* **44** R27
- [41] Moulton D., Corrigan G., Harrison J.R. and Lipschultz B. 2018 *Nucl. Fusion* **58** 096029
- [42] Brezinsek S. *et al* 2016 *Phys. Scr.* **T167** 014076
- [43] Fil A. *et al* 2020 *Plasma Phys. Control. Fusion* **62** 035008
- [44] Fil A. *et al* (EUROfusion MST Team T) 2022 *Nucl. Fusion* **62** 096026
- [45] Loarte A. 2001 *Plasma Phys. Control. Fusion* **43** 183–224
- [46] Chankin A.V., Delabie E., Corrigan G., Maggi C.F. and Meyer H. 2017 *Nucl. Mater. Energy* **12** 273–7
- [47] Jaervinen A.E. *et al* 2016 *Plasma Phys. Control. Fusion* **58** 045011
- [48] Giacomini M. *et al* 2021 *Nucl. Fusion* **61** 076002
- [49] Canik J.M. *et al* 2018 *IEEE Trans. Plasma Sci.* **46** 1081–5
- [50] Lunt T. *et al* 2015 *J. Nucl. Mater.* **463** 744–7
- [51] Aho-Mantila L. *et al* 2017 *Plasma Phys. Control. Fusion* **59** 035003
- [52] Jaervinen A.E. *et al* 2018 *Nucl. Mater. Energy* **19** 230–8
- [53] Reimold F. *et al* 2015 *J. Nucl. Mater.* **463** 128–34
- [54] Potzel S. *et al* 2014 *Nucl. Fusion* **54** 013001
- [55] Potzel S. *et al* 2015 *J. Nucl. Mater.* **463** 541–5
- [56] Reimold F. *et al* 2017 *Nucl. Mater. Energy* **12** 193–9
- [57] Dunne M.G. *et al* 2017 *Plasma Phys. Control. Fusion* **59** 014017
- [58] Dunne M.G. 2016 *Nucl. Fusion* **57** 025002
- [59] Wiesen S. *et al* 2017 *Nucl. Mater. Energy* **12** 3–17
- [60] De La Cal E. *et al* 2020 *Plasma Phys. Control. Fusion* **62** 035006